

Simulation and Analysis of Corona Currents in Large Scale Coaxial Geometry due to Triangular Voltages

by

Georgii Karman

Diploma work No. 123/2013

Department of Materials and Manufacturing Technology

Division of High Voltage Engineering

CHALMERS UNIVERSITY OF TECHNOLOGY

Gothenburg, Sweden

Diploma work in the Master Program ELECTRIC POWER ENGINEERING

Performed at: **Chalmers University of Technology**
SE-412 46 Gothenburg, Sweden

Supervisor/Examiner: Associate Professor Yuriy Serdyuk
Department of Materials and Manufacturing Technology
Division of High Voltage Engineering
Chalmers University of Technology
SE-412 46 Gothenburg, Sweden

Simulation and Analysis of Corona Currents in Large Scale Coaxial Geometry due to Triangular Voltages

GEORGII KARMAN

© GEORGII KARMAN, 2013

Diploma work no. 123/2013

Department of Materials and Manufacturing Technology

Division of High Voltage Engineering

Chalmers University of Technology

SE-412 96 Gothenburg, Sweden

Telephone +46 (0)31-772 1000

Cover:

Corona current-voltage characteristics for multiple frequencies of triangular voltage.

Chalmers Reproservice

Gothenburg, Sweden 2013

Simulation and Analysis of Corona Currents in Large Scale Coaxial Geometry due to Triangular Voltages

GEORGII KARMAN

Department of Materials and Manufacturing Technology

Division of High Voltage Engineering

Chalmers University of Technology

Abstract

Charged species can be generated in air due to corona discharges from sharp electrodes. They are of great concern in practical applications due to their ability to drift in the electric field and to accumulate on dielectric surfaces modifying electric field distributions. To understand better regularities of dynamic behavior of charge carriers produced by corona, series of experiments have been conducted at ABB Corporate Research Center in Västerås, Sweden. For this, a coaxial large scale electrode arrangement was utilized. Corona discharges were initiated by applying triangular voltages that allowed for studying drift of ionic species under controlled conditions. The experimentally obtained data required physical interpretation and this was the main objective of the present MSc thesis work.

In the thesis, a computer model of corona discharges in air is presented and its implementation in COMSOL Multiphysics is described. The developed model is utilized for simulations of corona discharges in the set-up used in the experiments. The computed current-voltage characteristics are compared with the experimental results. Influences of different model parameters, including the effect of boundary conditions, on corona characteristics are studied and a set of parameters providing the best fit between experiments and simulations is identified. An analysis of physical processes in corona discharges in air under triangular voltages at frequencies 1-50 Hz is presented focusing on interpretation of experimentally observed phenomena.

Keywords: AC corona, corona discharge, large scale coaxial electrodes, triangular voltage, corona mechanism, corona model for simulations, corona discharge current, corona current-voltage characteristic.

Acknowledgement

I would like to express my sincere appreciation to my supervisor, Docent Yuriy Serdyuk for immense support throughout the days of seemed everlasting confusion, especially in the beginning of thesis work; for his encouragement and guidance.

I would like to thank Olof Hjortstam, Joachim Schiessling and Nils Lavesson from ABB Corporate Research for giving me the opportunity to visit ABB research center and lab facilities, for providing me with the research data and for the fruitful discussions on the topic.

I would like also express my gratitude to Docent Jörgen Blenow for close look at my thesis results delivered at the presentation and setting the questions that I was pleased to give answers to.

Finally, special thanks go to my parents for giving me all the opportunities for my personal development.

Georgii Karman
Gothenburg, Sweden, 2013

Contents

Abstract	3
Acknowledgement	5
Contents	7
1 Introduction	1
1.1 Corona background	1
1.2 Overview of corona mechanisms in air	1
1.3 Research objectives	4
2 Experiments on corona in air under alternating voltages	7
2.1 Corona at power frequency and other types of stresses	7
2.2 Corona under triangular voltages	7
3 Model description	11
3.1 Hydrodynamic (drift-diffusion) model	11
3.2 Calculation of discharge current	13
3.3 Selection of input parameters	14
3.4 Computer implementation	17
3.5 Computational domain and model settings	20
4 Simulations of corona discharges in a large scale geometry	23
4.1 Model validation	23
4.2 Sensitivity to variations of input parameters	28
4.3 Corona current-voltage characteristics: experiment vs. simulation	32
5 Conclusions	37
5.1 Future work	38
References	39
Appendices	41

Chapter 1

Introduction

1.1 Corona background

Corona discharge is an electrical discharge usually accompanied by ripple noise and luminosity. This phenomenon appears in two or multi-electrode systems, providing non-uniform electric field, where at least one electrode is grounded and the other one is subjected to high potential. The electric field established between electrodes must be high enough to cause ionization of the isolating media that surrounds high and ground potential electrodes. Under corona occurrence the formation of weakly ionized gas (plasma) takes place. The field distribution confines the ionization processes within ionization region, close to high potential electrode, whereas the remaining region between two electrodes is dominated by electron and ion drift and conversion processes.

For the study purpose, corona discharge is commonly obtained in strongly non-uniform electric fields created by rod-plane or coaxial cylinder electrode geometries. This type of discharges may also appear in high-voltage apparatus being exposed to high voltage stresses. It is rather due to poor design that leads to equipment malfunction and eventually to permanent failure. Audible and radio-frequency noise is another undesirable effect of the corona. In the indoor installations, ozone and NO_x generated in air as by-products of corona, may also endanger humans lives.

1.2 Overview of corona mechanisms in air

Corona discharge occurs due to self-sustained electron avalanche development under high voltages in an atmospheric gas. High electric field at one of the electrodes above an ionization threshold causes decomposition of the air atoms into charge carrying ions, electrons and metastable molecules. The inter-electrode space is then divided into two regions, namely ionization and particle drift regions. The thickness of ionization region as well as particle drift and association in inter-electrode space depends on voltage polarity applied to the electrode of small curvature (potential electrode) and electrode geometry. Thus, corona mechanism, studied as early as 1929, is distinguished for positive and negative DC voltages as well as for AC voltages. The overview of each corona mechanism are to be presented in this Section.

The positive DC corona may exist in several forms: burst pulsation, steady glow, onset

streamer and breakdown streamer [1]. Among all these corona forms the burst pulsation is the corona initiation stage that disappears if applied voltage goes below the onset value. Increasing voltage from the burst pulsation stage leads to self-sustained corona discharge characterized by electron avalanches in ionization region. These electron avalanches excite gas atoms and molecules on its way towards anode. The excited atoms and molecules turning into a stable form emit photons that give luminous effect of a discharge process as well as cause secondary electron avalanche emission by photoionization. The discharge process near the anode gives rise to a cloud of positive ions that drift towards cathode but their continuous production rate in ionization region forms a positive space charge that decreases electric field strength at the anode. The electrons and negative ions in positive corona are swept immediately into the anode. For burst pulsation corona form it means extinction of ionization processes due to electric field strength below the ionization level. Once the positive space charge is swept away from the anode, another burst of discharge will take place in reestablished ionization region. The further increase in voltage will lead to space charge accumulation near the anode. The electric field between positive space charge and anode surface reduces significantly whereas the front of this space charge creates relatively high electric field strength so that it establishes another ionization region nearby. As a result, new electron avalanches will grow in front of the space charge and plasma channel will develop towards the cathode. This plasma channel is luminous and is otherwise known as streamer. With the streamer development the ionization region propagates towards the cathode. At a certain distance from the anode the weakened electric field strength establishes the border between ionization and drift region. In the drift region no electron avalanche development takes place and only recombination and attachment of ions and electrons is dominant. The electrons that appear due to background natural processes will be attached to the positive drifting ions neutralizing the space charge. However, the complete vanishing of the space charge depends on the background ionization rate.

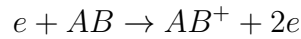
Further increase in voltage will create conditions for glow corona discharge. It occurs when burst pulses merge and become no longer distinguishable. One prominent characteristic of a glow corona is the constant electric field strength at the anode surface irrespective of further increase in voltage until breakdown streamer voltage threshold is reached. The breakdown streamers develop for longer distances and may eventually cause the breakdown of the air gap between electrodes. It happens when streamer touches the surface of the cathode.

The negative corona mechanism is similar to the positive one with some minor differences. It may also exist in several forms: Trichel pulses (named after G. V. Trichel who first studied this form of corona), negative glow, negative or positive streamer [1]. With the negative voltage applied to the small curvature electrode the established electric field accelerates positive ions towards the cathode (high potential electrode) and repels electrons and negative ions towards the anode. In the ionization region electrons associate with excited atoms and molecules producing new electrons multiplying in avalanches. It is also known that secondary ionization process in negative corona exists in which emission of electrons occurs by impact of positive ions and photons bombarding the cathode surface. By nature, negative ions exist only in electronegative gases such as atmospheric air. This is due to ability of oxygen molecules to attach electrons in low electric field drift region forming the negative ions. The negative space charge accumulating in the drift re-

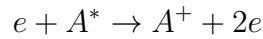
gion reduces electric field strength in ionization region. So, for the initial corona Trichel pulses it causes the discharge extinction. Another ionization process will take place only when the cloud of negative space charge drifts away from the cathode. With an increase in voltage all the aforementioned negative corona forms transit from one stage to another as was described for the positive corona mechanism. In the transition from the glow form to the spark breakdown the negative streamers may appear right after the positive streamers. This negative streamers develop towards the anode out of the glow corona region.

Both negative and positive DC corona inherent processes of particles association consist of the same composition. This composition embraces ionization, attachment, recombination and detachment processes. These so called particle production and loss processes are numerously studied and presented in a wide range in field of corona discharges. However, for simplicity and model accuracy reasons the processes listed below are considered fundamental.

Ionization in discharge plasma may be described as the electron-atom or molecule collision in which the following reaction takes place

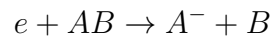


Another possible electron association with an excited particle is described in the following relation



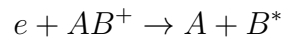
The ionization process in plasma may be triggered by photons as well. However, for simplicity reasons, photons will not be treated in this research.

The discharge in electronegative gas such as air would be always accompanied by formation of the negative ions. This is due to ability of the oxygen molecules to attach free electrons. The attachment process may be described by the following relation



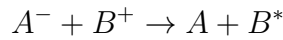
For the atmospheric pressure air the attachment process usually involves three bodies association (electron, oxygen and impurity gas molecules present in air) instead of two (electron and oxygen molecule) for low pressures.

The electron-ion dissociative recombination process contributes to electrons and positive ions loss in the corona plasma. It is described as follows



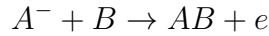
For atmospheric pressure air, electron-ion recombination occurs primarily in two body collision whereas for high pressures it may involve three bodies. Electron disappearance may also occur in radiative electron-ion recombination that plays major role in highly ionized spark channels. In this project, however, dissociative recombination of electrons and ions will be considered only.

The ion-ion recombination involving positive and negative ions, similar to the electron-ion recombination, may occur either in two or three body association. The rate of ions association is pressure and temperature dependent [1]. For the current study the following two body ion-ion recombination process will be considered

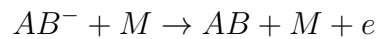


The excess of energy in such two body collision is absorbed by one of the ions in transition to the excited state.

The inverse process for attachment is the electron detachment. It may be of three different origins. First one is an associative detachment, when electron is produced out of the oxygen ion and oxygen atom or carbon dioxide molecule reaction



Another origin is for collisional detachment, when ion and neutral particle collide producing electron



Finally, photodetachment described first time by Massey in 1938 may be considered as the secondary feedback mechanism in electron production and negative ion loss process. Many authors have given rather versatile conclusions regarding detachment processes in air plasma. Therefore, for the simulation model used in this research, necessary approximations will be stated.

Talking about particles movement when subjected to an electric field, two distinctive transport mechanisms affect the electrons and ions relocation, namely drift and diffusion. Drift of electrons and ions is a transport of mass, parallel to an electric field vector lines and with a velocity proportional to an electric field. In a positive electric field electrons and negative ions as carriers of negative charge drift towards anode (potential electrode) whereas positive ions drift towards cathode (grounded electrode). The opposite direction of particle drift occurs in a negative electric field. Diffusion is a natural phenomena of particle redistribution from the region of higher concentration to the region of lower concentration. In mathematical model it is characterized by diffusion coefficient being negative gradient of the particle concentration.

1.3 Research objectives

To understand physical mechanisms and to explain the results obtained experimentally, computer modeling of the corona discharges is to be conducted in the present MSc thesis work. It is expected that the developed computer models, being verified against the experimental data, will provide an accurate description of the corona physics for the specified conditions. The overall analysis and mathematical description of the simulation model will be of great use for solving large scale HV equipment design problems.

In order to build successful corona simulation model that will allow to analyze the corona measured data for large scale coaxial cylindrical system the following steps will be undertaken in the scope of this thesis:

- Studying existing corona modelling approach
- Developing a computer model

- Simulations of corona under triangular voltages in the large scale electrode system
- Verification of the simulation results against measured corona currents
- Investigation of parameters affecting corona currents

Chapter 2

Experiments on corona in air under alternating voltages

2.1 Corona at power frequency and other types of stresses

The AC corona is usually considered as the power frequency corona in the range of 1-60 Hz alternating voltages. High-frequency corona studies are also of particular interest in scientific world, however, are not to be discussed in the current thesis.

Alternating voltages give rise to corona discharge currents as frequency and space charge build-up [2]. The magnitude and the distribution of the latter are changing in time with the change of voltage polarity. Moreover, the space charge movement under alternating voltages is registered as the displacement current in addition to the conduction current. Apart from displacement current, the change of voltage derivative in time causes capacitive current component defined by the geometrical capacitance of the system.

The frequency of the applied voltage and the gap length between two electrodes play major role in shaping AC corona discharge currents. If either frequency or inter-electrode distance makes electrons and ions unable to cross the gap in half a cycle, the accumulation of a space charge will take place leading to field distortion and lowering of corona onset voltage [2]. If electrons and ions have sufficient time to traverse the gap between electrodes, the discharge behavior would be similar to one under static conditions. This way, the field distribution would become more uniform and recombination losses would increase due to longer time of particle association in the drift region.

2.2 Corona under triangular voltages

Series of experiments have been conducted recently at ABB Corporate Research (Västerås, Sweden) to investigate behavior of space charges in corona under well-controlled conditions. For this, discharges were arranged in a large scale coaxial electrode system with dimensions, which are of interest for industrial applications. The inner electrode used was a thin wire of diameter $d = 0.26$ mm. As an outer electrode the cylindrical metallic cage was used with diameter $D = 1000$ mm. Additional outer cage of the diameter $D_{out} = 2.5$ m was used for noise elimination in the measurements. The height of the coaxial system was 2.5 m. With such electrodes dimensions the highly inhomogeneous electric field distribu-

tion was achieved. The measurement of the current at the outer grounded electrode was performed by Keithley electrometer 6517A and was recorded using LeCroy oscilloscope. The principal drawing of the experimental system set-up is shown in Fig. 2.1.

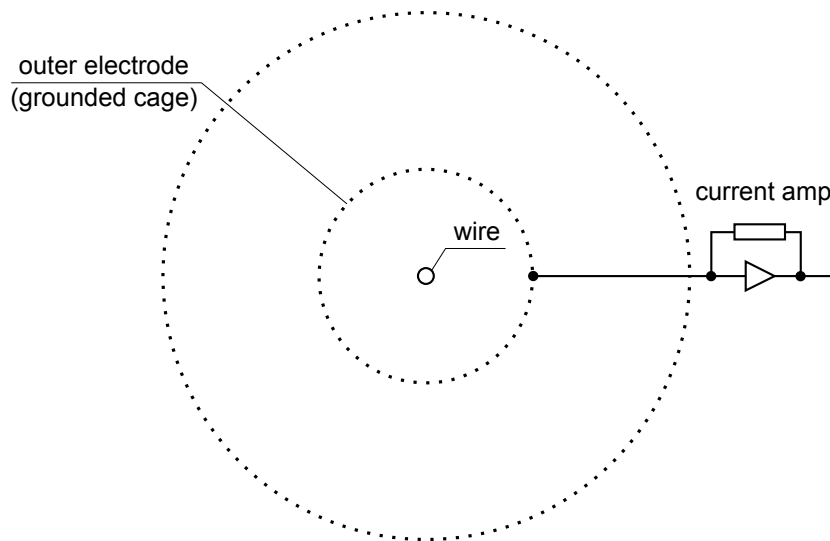


Fig. 2.1 Coaxial electrode setup for experiment

Although the experiment on coaxial arrangement has been conducted with the test voltages of DC and AC origin, the latter with varied frequency range from 1 Hz to 50 Hz is of particular interest for the current research. The AC voltage applied to the wire was of triangular shape and of 20 kV magnitude. This way, the constant grow and decay rate of the potential made it possible to use the recorded current-voltage characteristics for an accurate analysis in the simulation stage. The current-voltage characteristics of selected frequencies are shown in Fig. 2.2.

As seen, the triangular shape voltage applied to the coaxial electrode system results in “butterfly-like” shape of the current-voltage characteristic of the AC corona discharge.

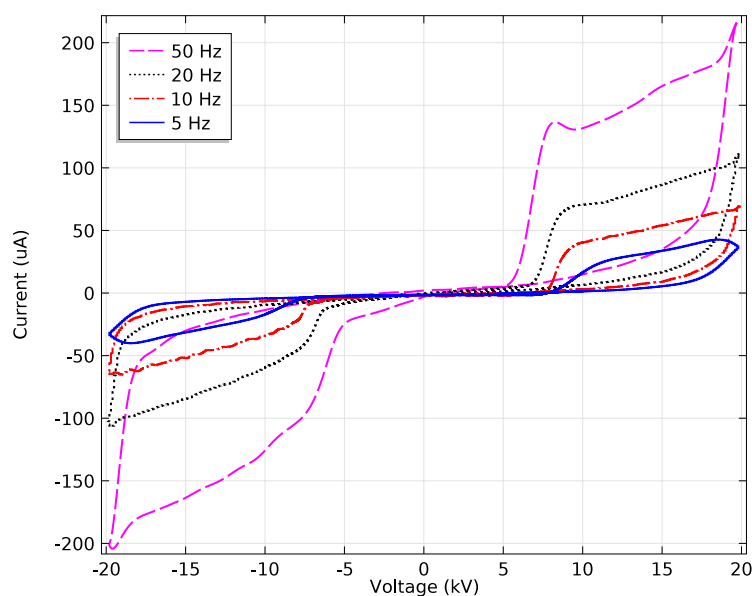


Fig. 2.2 Current-voltage characteristics obtained in the experiment

It is clearly illustrated that the higher the frequency, the lower the corona onset voltage. This effect is caused by space charge accumulation and thus enhancement of the electric field at the wire [2]. Besides the higher magnitude of the current, the bump at the positive half period (in the transition between steep current rise and its flattening) is observed which becomes more pronounced at higher frequencies.

The presented records of AC corona currents will be further used in simulation stage as the material to study and analyze the charge carriers dynamics by means of different characteristic dependencies plotted in time, space and electric field domains. Ultimately, the match of experimental current-voltage characteristics and the ones obtained in simulation is expected by adjusting the corona model parameters.

Chapter 3

Model description

3.1 Hydrodynamic (drift-diffusion) model

In this section the general approach of corona discharge modelling is to be described. For simplicity reason all the relations that embrace the empirically obtained parameters and their references are to be presented in section 3.3.

The physical system of corona discharge can be described by balance equation. The general form of such equation is as follows

$$\frac{\partial n}{\partial t} + \nabla \cdot \Gamma = S \quad (3.1)$$

where n stands for particle species density, Γ stands for flux and S is the source term. All the variables stated in (3.1) are functions of space and time.

The flux Γ in (3.1) consists of two terms, namely drift and diffusive fluxes.

$$\Gamma = \mu E n - D \nabla n \quad (3.2)$$

The drift flux in (3.2) is characterized by the particle mobility μ and is proportional to the applied electric field E . Diffusive term in (3.2) is characterized by gradient of the particle density and the diffusion coefficient D .

The source term in (3.1) accounts for multiple reactions that take place in corona plasma. In these reactions, particles are either created or destroyed. Each reaction would be described later considering particular particle species.

Summarizing continuity equation for each particle species and taking behavior of the particle fluxes into account, the final hydrodynamic model can be described by three equations as follows

$$\frac{\partial n_e}{\partial t} + \nabla \cdot (-n_e w_e - D_e \nabla n_e) = S_e \quad (3.3)$$

$$\frac{\partial n_p}{\partial t} + \nabla \cdot (n_p w_p - D_p \nabla n_p) = S_p \quad (3.4)$$

$$\frac{\partial n_n}{\partial t} + \nabla \cdot (-n_n w_n - D_n \nabla n_n) = S_n \quad (3.5)$$

where e, p and n subscripts denote electrons, positive and negative ions respectively; w is the product of μE which gives the particle drift velocity in the field applied.

The diffusion coefficient for positive and negative ions in (3.2) is defined by the following relation

$$D = \mu k_B \frac{T}{q} \quad (3.6)$$

where T is the corresponding ion temperature, k_B is the Boltzmann constant and q is the elementary charge. The field dependent ion temperature can be evaluated by the following relation

$$k_B T = k_B T_g + \frac{1}{3}(m_i + m)w_i^2 \quad (3.7)$$

here, m_i and m are ion and molecule masses respectively, T_g is the air temperature and w is the ion drift velocity in an electric field.

The diffusion coefficient D_e for electrons is used as in tabulated values for a specific reduced electric field E/n and interpolated for the whole range of electric field values established between electrodes. The reference values of diffusion coefficient are given in Appendix A.

Since electric field between electrodes will experience distortion by the space charge accumulation in an inter-electrode space, it is to be calculated solving the Poisson equation

$$\nabla \cdot (\varepsilon \nabla \phi) = -q(n_p - n_e - n_n) \quad (3.8)$$

where ε is the absolute permittivity of an air.

$$E = -\nabla \phi \quad (3.9)$$

Source terms in (3.3), (3.4) and (3.5) as was mentioned earlier, are the sums of the relevant reactions during which particle species are created or destroyed. Even though there are tens or even hundreds of reactions that occur in corona process, some of these reactions dominate over the others. Therefore, for each charged species the following approximation holds true

$$S_e = R_0 + R_{ion} + R_{det} - R_{rec}^{ei} - R_{att} \quad (3.10)$$

$$S_p = R_0 + R_{ion} - R_{rec}^{ii} - R_{rec}^{ei} \quad (3.11)$$

$$S_n = R_{att} - R_{det} - R_{rec}^{ii} \quad (3.12)$$

here, R_0 is the rate of background ionization, R_{ion} is the rate of ionization, R_{det} is the rate of electron detachment from the negative ion when latter collides with a gas molecule, R_{att} is the rate of electron attachment to the neutral particle that gives birth to negative ion, R_{rec}^{ei} is the electron-ion recombination rate and R_{rec}^{ii} is the same for ion-ion recombination.

Each of the reactions mentioned are the products of the reacting particle densities and the rate coefficient. Thus, the rate of ionization is calculated as follows

$$R_{ion} = \alpha n_e w_e \quad (3.13)$$

here, α is the first ionization coefficient tabulated values of which are given in the appendix.

The rate of electron attachment in turn is the product of the attachment coefficient, electron density and electron velocity. The attachment coefficient η is also given in the appendix.

$$R_{att} = \eta n_e w_e \quad (3.14)$$

Rates of ion-ion and electron-ion recombination are calculated by the following relation

$$R_{rec}^{ii} = \beta_{ii} n_p n_n \quad (3.15)$$

$$R_{rec}^{ei} = \beta_{ei} n_e n_p \quad (3.16)$$

where β_{ii} and β_{ei} are the ion-ion and electron-ion recombination coefficients respectively.

The last significant reaction in corona plasma is the rate of electron detachment from the negative ions. It is calculated as follows

$$R_{det} = k_{det} N n_n \quad (3.17)$$

here, k_{det} is the detachment coefficient, N is the gas density. Multiplying by the gas density in (3.17) the detachment of electrons due to collision of negative ions with gas molecules is considered.

Some of the parameters in the model depend on the air pressure and temperature. These are gas density N and ion mobilities μ_p and μ_n . Therefore, the following holds true for gas density

$$N = \frac{P}{k_B T} \quad (3.18)$$

where pressure P is given in [Pa] and temperature T is in [K].

The ion mobilities values, in turn, need to be divided by relative air density δ calculated as follows

$$\delta = \frac{T_0 P}{T P_0} \quad (3.19)$$

here, T_0 and P_0 are reference values of temperature and pressure, whereas T and P are their current values.

3.2 Calculation of discharge current

The current that is measured at the grounded electrode consists of several terms. The first, called conductive, is caused by movement of particles crossing the inter-electrode distance and flowing into the ground through the amperemeter. It is described as follows

$$A \cdot q \cdot E(n_p \mu_p - n_e \mu_e - n_n \mu_n) = I_{cond} \quad (3.20)$$

where A is the area of the grounded electrode.

Another term contributing to the total current is the displacement current. This current itself may be divided into two contributing terms, namely capacitive term and charge term. The former exists only if the time derivative of the applied voltage is greater than zero. The latter exists when moving particles are present in the air gap between electrodes that causes the variation of electric field. These two displacement current components are described as follows

$$C \frac{dU}{dt} = \frac{2\pi \cdot H}{\ln(R/r)} \frac{dU}{dt} = I_{cap} \quad (3.21)$$

$$A \cdot \left(\varepsilon \frac{\partial E}{\partial t} \right) = I_{disp} \quad (3.22)$$

Thus, the actual total current that can be measured at the electrode is the arithmetic sum of three contributing terms

$$I_{total} = I_{cond} + I_{disp} - I_{cap} \quad (3.23)$$

3.3 Selection of input parameters

Numerous scientific publications are available today being the source for corona model parameters. These parameters (ion mobilities, rates of recombination, electron mean energies, etc.) have been extensively studied so that their accurate values is just a matter of choice. Therefore, all of the parameters and constants given in this section have been selected on first choice basis with intention to alter them for the best fit of experimental results into the simulation ones.

To begin with, the field-dependent electron characteristics in air can be analyzed for selection purposes. There are definitely discrepancies among different author's stating the experimentally obtained electron characteristics data. These discrepancies may be no more than just a consequence of different equipment used and calculation techniques. Some authors [3] [4], however, are considered to give the most reliable data that have been adopted for the current studies.

Yet another problem in selecting the right electron field-dependent characteristics lies within the value of air humidity for which these parameters had been obtained. Humidity of air increases attachment of electrons in corona plasma thus reducing the intensity of corona and altering an onset voltage [5] [6]. It also affects the ionization coefficient and electrons drift velocity [6] [7]. Later, considering humid air as a mixture of dry air and water vapour, the mathematical approach to derive exact electron parameters for different relative air humidity values had been proposed [8] [9] [10]. In order to use this approach in current studies the electron parameters for dry air and water vapour must be available in broad range of electric field. Unfortunately, the attempts to conduct such measurements in water vapor were made for narrow ranges of electric field, not applicable to current

studies. Therefore, the approximation will be stated here to treat the air dry for all the electron parameters used further.

The reduced ionization (α/N) and attachment (η/N) coefficients, electron drift velocity (w_e) and characteristic energy (D/μ) as functions of reduced electric field are reproduced in Fig. 3.1 through 3.3. The tabulated values of these parameters are given in Table 1, Appendix A. They will be used in derivation of α , η , electron mobility μ_e and electron diffusion coefficient D_e for the given stresses in the inter-electrode space.

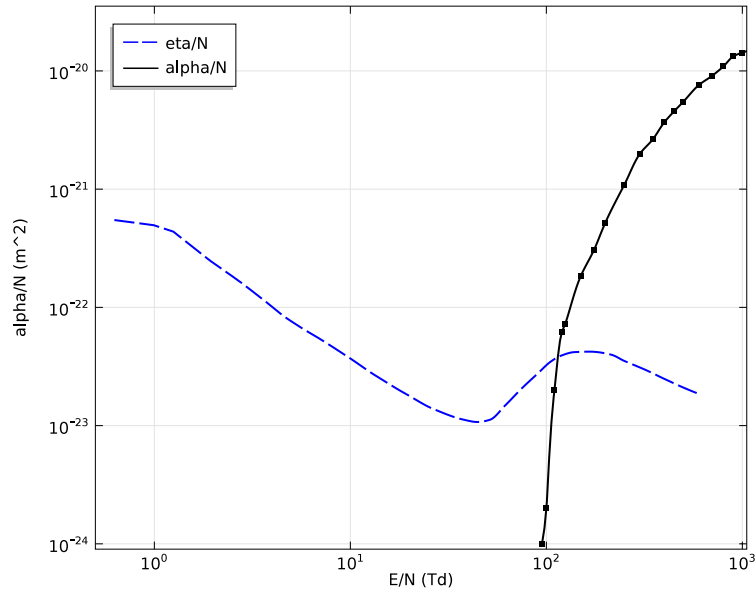


Fig. 3.1 Calculated values of α/N and η/N as a function of E/N for dry air

The Townsend breakdown mechanism incorporates secondary ionization coefficient γ (for negative corona). This coefficient is the fraction of the positive ions bombarding the cathode and thus dislodging new electrons out of the cathode surface.

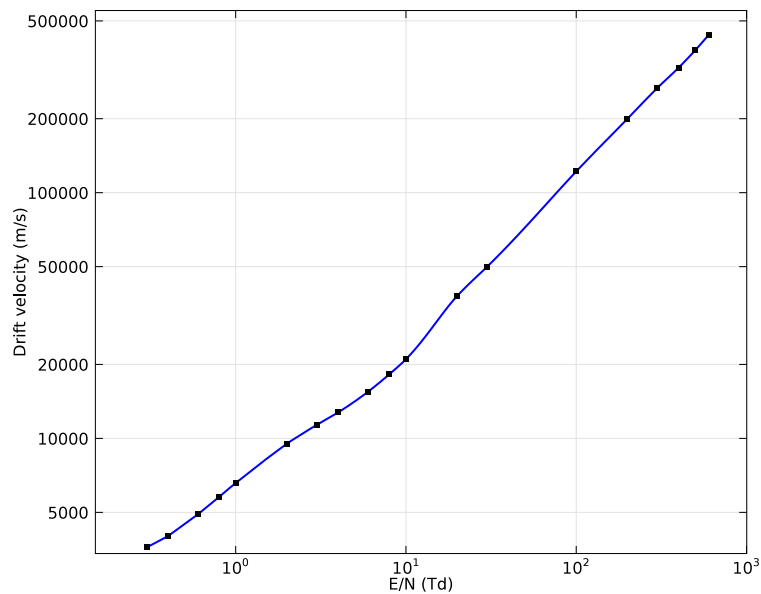


Fig. 3.2 Calculated values of electron drift velocity as a function of E/N for dry air

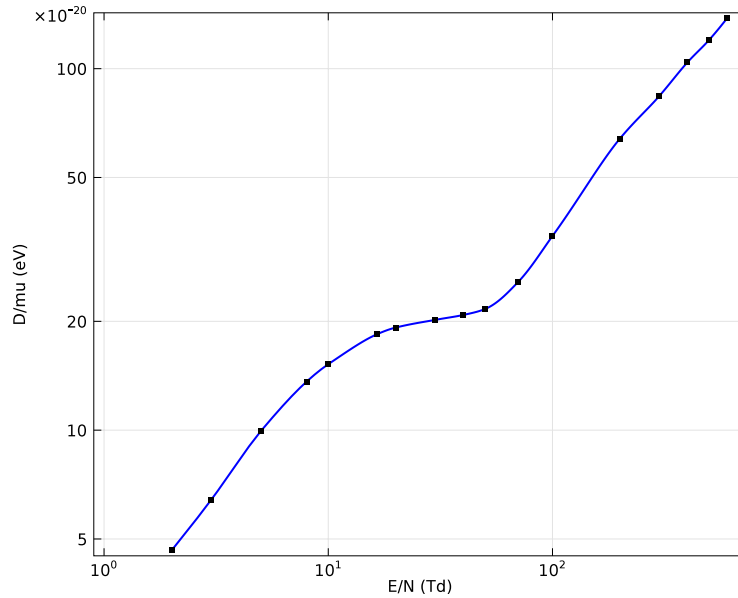


Fig. 3.3 Calculated values of electron characteristic energy D/μ as a function of E/N for dry air

It may also be a result of metastable molecules bombardment of a cathode or even photoeffect caused by photons. Studies presented in [11] suggest that γ strongly depends on electrode material and its surface roughness. Whereas common values for γ are scattered within 10^{-3} to 10^{-4} range, some authors suggested γ to be less than 10^{-4} . Therefore, this coefficient value is to be verified and model sensitivity to variations of γ coefficient is to be presented in Section 4.2.

Ion mobilities are considered to be independent of electric field [12]. According to [12], mobilities of positive and negative ions are $2.0 \cdot 10^{-4}$ and $2.7 \cdot 10^{-4}$ $\text{m}^2/\text{V}\cdot\text{s}$ respectively. Another research [13] has revealed the average ion mobilities to be $1.36 \cdot 10^{-4}$ and $1.56 \cdot 10^{-4}$ $\text{m}^2/\text{V}\cdot\text{s}$ for positive and negative species respectively. Therefore, these mobility values are also to be verified at the simulation stage.

The ion-ion recombination rate is defined by the following relation [14]

$$\beta_{ii} = 2 \cdot 10^{-12} \left(\frac{300}{T_i} \right)^{1.5} [m^{-3}s^{-1}] \quad (3.24)$$

where ion temperature T_i can be calculated by (3.7).

For the electron-ion recombination rate in (3.16), different recombination coefficients exist depending on whether ions are of simple (N_2^+ , O_2^+ , NO^+) or complex (N_4^+ , O_4^+ , N_2O_2^+) structure [15]. The ions of simple structure give $\beta_{ei} = 5 \cdot 10^{-14}$ $\text{m}^{-3}\text{s}^{-1}$ coefficient. This value will be considered in current studies.

The ion-molecule association in corona plasma gives electron detachment from negative ions with the rate determined in (3.17). The detachment coefficient in (3.17) is defined as follows [16]

$$k_{det} = 2 \cdot 10^{-16} \exp \left(-\frac{6030}{T_i} \right) [m^{-3}s^{-1}] \quad (3.25)$$

where T_i is accounted for by (3.7).

All of the parameters covered in this Section are basically the variables that are to be

verified and sensitivity analysis is to be made in order to investigate their contribution to the simulation results.

3.4 Computer implementation

In this section all the aspects of corona modelling in finite-element package COMSOL Multiphysics is presented. For the reasons of flexibility and ease of model parameters handling, COMSOL Multiphysics is considered the number one choice for coupled partial differential equations problem solving. For the computer simulation, the version 4.3a of COMSOL Multiphysics was used, thus all the stages and examples of the model implementation would be explained accordingly.

At the initiation of a multiphysics problem set-up one should carefully consider the dimensionality of a problem. In case of cylindrical coaxial electrode geometry the problem can be accurately resolved in 1D axisymmetrical domain. This way, the left and the right boundaries of the computational domain will represent the surfaces of the coaxial electrodes whereas the whole line connecting in between will represent the air where all the corona discharge processes develop.

To begin with, in the *Model Wizard* window the *1D axisymmetric* space dimension must be selected. At the stage of adding physics, *Electrostatics* interface in *AC/DC* module should be selected solving for (3.8) together with *Transport of Diluted Species* interface in *Chemical Species Transport* module, one for each equation (3.3)-(3.5). Finally, the *Time Dependent* study type must be selected.

After *Model Wizard* stage has been completed, one can switch to specifying the model geometry in *Model Builder* tab. In coaxial electrodes arrangement the computational domain is a straight line as shown in Fig. 3.4.

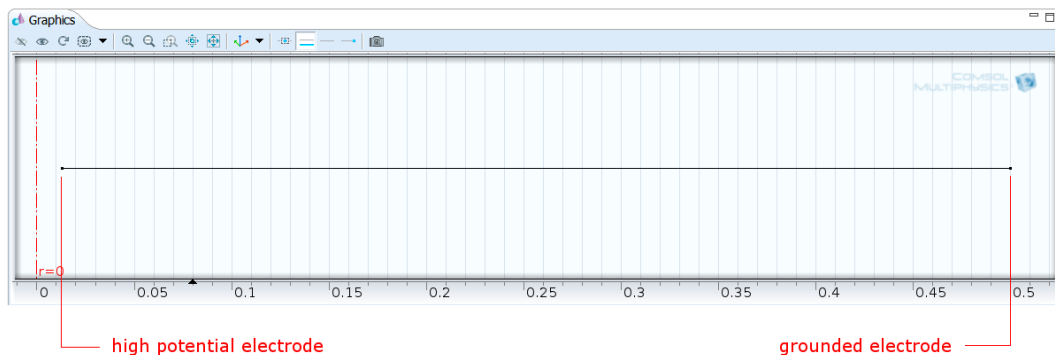
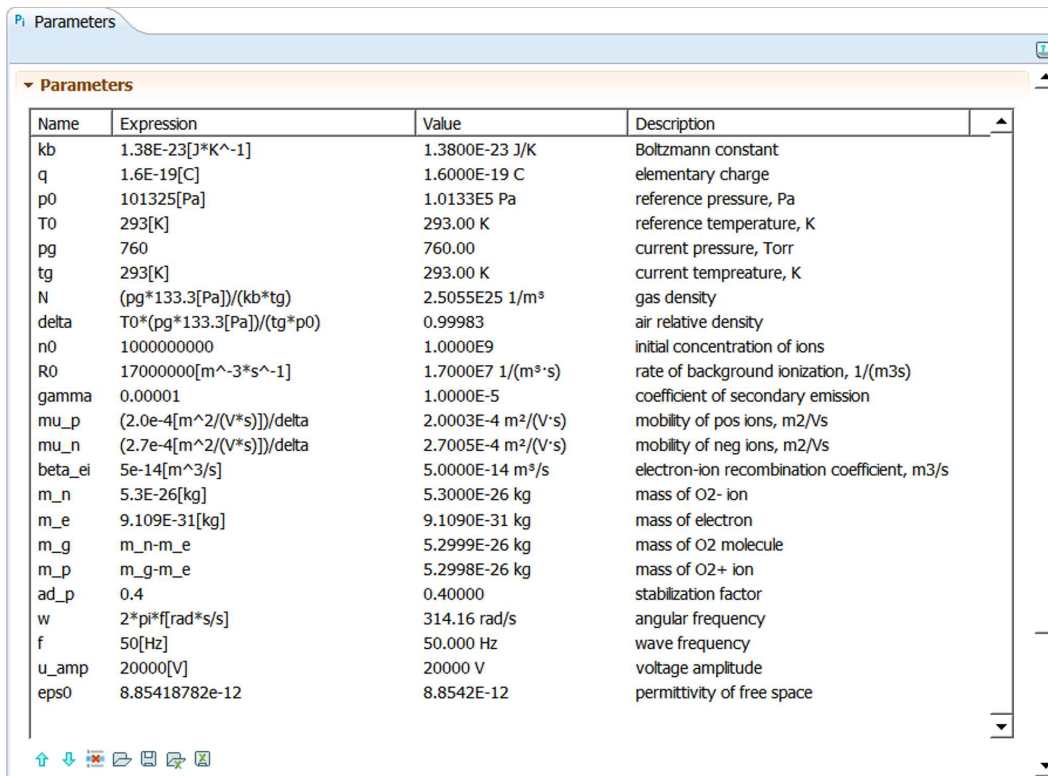


Fig. 3.4 1D axisymmetrical computational domain: coaxial cylindrical electrodes

For the convenience purpose, the dependent variables solved for in each *Transport of Diluted Species* interface can be renamed to *e*, *pos* and *neg* denoting concentration of electrons, positive and negative ions respectively. It is also important to change to *Conservative form* in *Advanced Settings* tab provided that advanced physics options are shown in the model window. The conservative form option makes the drift flux term in (3.2) appear under differential operator as in (3.1).

Next step is to specify the model parameters. This is done by creating a group of nodes in *Global Definitions* branch. Here, node *Parameters* will contain all the constants provided for the model as shown in Fig. 3.5.



Name	Expression	Value	Description
kb	$1.38E-23[J*K^{-1}]$	1.3800E-23 J/K	Boltzmann constant
q	$1.6E-19[C]$	1.6000E-19 C	elementary charge
p0	$101325[Pa]$	1.0133E5 Pa	reference pressure, Pa
T0	$293[K]$	293.00 K	reference temperature, K
pg	760	760.00	current pressure, Torr
tg	$293[K]$	293.00 K	current temperature, K
N	$(pg*133.3[Pa])/(kb*tg)$	2.5055E25 1/m ³	gas density
delta	$T0*(pg*133.3[Pa])/(tg*p0)$	0.99983	air relative density
n0	1000000000	1.0000E9	initial concentration of ions
R0	$17000000[m^{-3}*s^{-1}]$	1.7000E7 1/(m ³ *s)	rate of background ionization, 1/(m ³ s)
gamma	0.00001	1.0000E-5	coefficient of secondary emission
mu_p	$(2.0e-4[m^2/(V*s)]/delta)$	2.0003E-4 m ² /(V*s)	mobility of pos ions, m ² /Vs
mu_n	$(2.7e-4[m^2/(V*s)]/delta)$	2.7005E-4 m ² /(V*s)	mobility of neg ions, m ² /Vs
beta_ei	$5e-14[m^3/s]$	5.0000E-14 m ³ /s	electron-ion recombination coefficient, m ³ /s
m_n	$5.3E-26[kg]$	5.3000E-26 kg	mass of O2- ion
m_e	$9.109E-31[kg]$	9.1090E-31 kg	mass of electron
m_g	m_n-m_e	5.2999E-26 kg	mass of O2 molecule
m_p	m_g-m_e	5.2998E-26 kg	mass of O2+ ion
ad_p	0.4	0.40000	stabilization factor
w	$2*pi*f[rad*s/s]$	314.16 rad/s	angular frequency
f	$50[Hz]$	50.000 Hz	wave frequency
u_amp	$20000[V]$	20000 V	voltage amplitude
eps0	$8.85418782e-12$	8.8542E-12	permittivity of free space

Fig. 3.5 Model parameters in Global Definitions menu

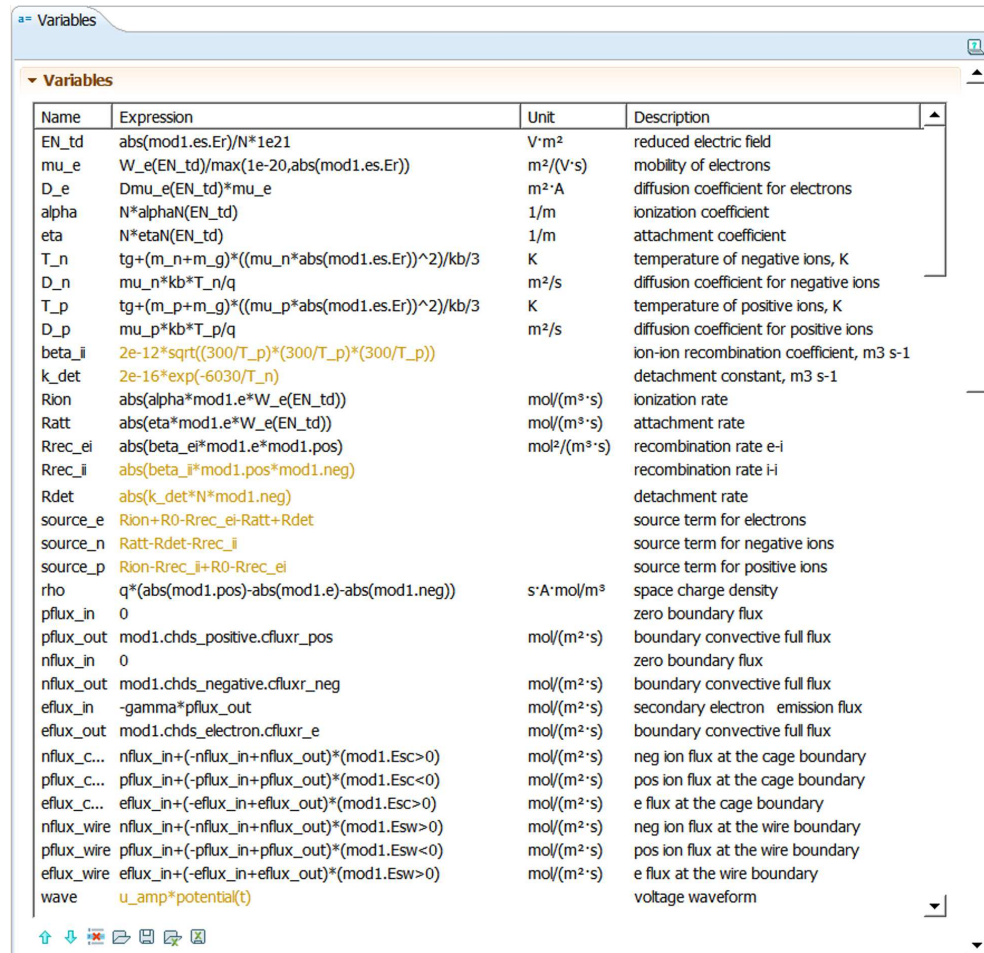
Another node *Variables* shown in Fig. 3.6 will contain all the parameters and expressions that directly or indirectly depend on electric field. Thus, the COMSOL in-built variable name $es.normE$ from *Electrostatics* interface is used to build such expressions. The boundary conditional expressions that formulate the field dependent direction of a particle conductive flux can be also defined in the *Variables* node.

Some of the variables such as α and η coefficients, electron velocity w and electron diffusion coefficient D_e used in (3.3) and (3.13)-(3.14) are to be calculated from the available functions where reduced electric field E/N , Td is an argument. For this purpose, tabulated values of ionization $\alpha/N(E/N)$ and attachment $\eta/N(E/N)$ coefficients, characteristic energy $D_e/\mu_e(E/N)$ and electron drift velocity $w_e(E/N)$ can be defined as *Interpolation* functions in corresponding nodes. Configuring interpolation functions, the *Piecewise Cubic* interpolation and *Constant* extrapolation methods must be selected. During the problem computation stage the dependency of the results upon correct units for *Arguments* and *Function* fields in interpolation function set-up was noticed. The tabulated values of the variables defined as interpolation functions are given in the Appendix.

The last useful node to create at the *Global Definitions* branch is the *Waveform* function that can be greatly utilized for potential waveform applied to the high voltage electrode. This waveform function gives possibility to smooth the transition zone of the waveform where function derivative changes sign, for instance the triangular shape function. Otherwise, having sharp edges of the potential waveform would create computational instabilities.

Now that all the expressions, variables and parameters are defined, one can assign the corresponding names of the parameters in the default nodes *Convection and Diffusion* and *Initial Values* in *Transport of Diluted Species* interface. Then, create new nodes: *Reactions*, to specify the source for the particle, *Flux*, to assign the boundary conditional expression, one for each boundary. Repeat the procedure for the *Electrostatics* interface, specifying the parameters in *Electric Potential*, *Ground* and *Space Charge Density* nodes.

After configuring physics interfaces, the model geometry must be meshed with finite elements. Due to inhomogeneous distribution, the steep gradient of the electric field close to the high potential electrode is expected. Thus, most of the reactions and particle movements must be accurately resolved by mesh high resolution in this ionization region. The mesh density for the rest of the domain is preferred to be kept low. To achieve fine meshing, the *Distribution* node must be used in *Mesh* branch. This particular node makes it possible to create adaptive meshing through defining *Number of elements* field and then setting up *Element ratio* for the high potential electrode boundary to increase the distribution density at that boundary.



Name	Expression	Unit	Description
EN_td	$\text{abs}(\text{mod1.es.Er})/N*1e21$	V·m ²	reduced electric field
mu_e	$W_e(\text{EN_td})/\text{max}(1e-20,\text{abs}(\text{mod1.es.Er}))$	m ² /(V·s)	mobility of electrons
D_e	$\text{Dmu}_e(\text{EN_td})*\text{mu}_e$	m ² ·A	diffusion coefficient for electrons
alpha	$N*\text{alphaN}(\text{EN_td})$	1/m	ionization coefficient
eta	$N*\text{etaN}(\text{EN_td})$	1/m	attachment coefficient
T_n	$\text{tg}+(\text{m}_n+\text{m}_g)*((\text{mu}_n*\text{abs}(\text{mod1.es.Er}))^2)/\text{kb}/3$	K	temperature of negative ions, K
D_n	$\text{mu}_n*\text{kb}*T_n/q$	m ² /s	diffusion coefficient for negative ions
T_p	$\text{tg}+(\text{m}_p+\text{m}_g)*((\text{mu}_p*\text{abs}(\text{mod1.es.Er}))^2)/\text{kb}/3$	K	temperature of positive ions, K
D_p	$\text{mu}_p*\text{kb}*T_p/q$	m ² /s	diffusion coefficient for positive ions
beta_ii	$2e-12*\text{sqrt}((300/T_p)*(300/T_p)*(300/T_p))$		ion-ion recombination coefficient, m ³ s ⁻¹
k_det	$2e-16*\text{exp}(-6030/T_n)$		detachment constant, m ³ s ⁻¹
Rion	$\text{abs}(\text{alpha}*mod1.e*W_e(\text{EN_td}))$	mol/(m ³ ·s)	ionization rate
Ratt	$\text{abs}(\text{eta}*mod1.e*W_e(\text{EN_td}))$	mol/(m ³ ·s)	attachment rate
Rrec_ei	$\text{abs}(\text{beta_ei}*mod1.e*mod1.pos)$	mol ² /(m ³ ·s)	recombination rate e-i
Rrec_ii	$\text{abs}(\text{beta_ii}*mod1.pos*mod1.neg)$		recombination rate i-i
Rdet	$\text{abs}(\text{k_det}*N*mod1.neg)$		detachment rate
source_e	$Rion+R0-Rrec_ei-Ratt+Rdet$		source term for electrons
source_n	$Ratt-Rdet-Rrec_ii$		source term for negative ions
source_p	$Rion-Rrec_ii+R0-Rrec_ei$		source term for positive ions
rho	$q*(\text{abs}(\text{mod1.pos})-\text{abs}(\text{mod1.e})-\text{abs}(\text{mod1.neg}))$	s·A·mol/m ³	space charge density
pflux_in	0		zero boundary flux
pflux_out	$\text{mod1.chds_positive.cfluxr_pos}$	mol/(m ² ·s)	boundary convective full flux
nflux_in	0		zero boundary flux
nflux_out	$\text{mod1.chds_negative.cfluxr_neg}$	mol/(m ² ·s)	boundary convective full flux
eflux_in	$-\text{gamma}*pflux_out$	mol/(m ² ·s)	secondary electron emission flux
eflux_out	$\text{mod1.chds_electron.cfluxr_e}$	mol/(m ² ·s)	boundary convective full flux
nflux_c...	$\text{nflux_in}+(-\text{nflux_in}+\text{nflux_out})*(\text{mod1.Esc}>0)$	mol/(m ² ·s)	neg ion flux at the cage boundary
pflux_c...	$\text{pflux_in}+(-\text{pflux_in}+\text{pflux_out})*(\text{mod1.Esc}<0)$	mol/(m ² ·s)	pos ion flux at the cage boundary
eflux_c...	$\text{eflux_in}+(-\text{eflux_in}+\text{eflux_out})*(\text{mod1.Esc}>0)$	mol/(m ² ·s)	e flux at the cage boundary
nflux_wire	$\text{nflux_in}+(-\text{nflux_in}+\text{nflux_out})*(\text{mod1.Esw}>0)$	mol/(m ² ·s)	neg ion flux at the wire boundary
pflux_wire	$\text{pflux_in}+(-\text{pflux_in}+\text{pflux_out})*(\text{mod1.Esw}<0)$	mol/(m ² ·s)	pos ion flux at the wire boundary
eflux_wire	$\text{eflux_in}+(-\text{eflux_in}+\text{eflux_out})*(\text{mod1.Esw}>0)$	mol/(m ² ·s)	e flux at the wire boundary
wave	$u_amp*\text{potential}(t)$		voltage waveform

Fig. 3.6 Model variables in Global Definitions menu

Finally, the time-dependent solver must be configured for this specific problem. Some of the solver parameters are crucial to specify in order to compromise computational time and result accuracy. To begin with, several nodes in *Study* → *Solver Configurations* → *Solver* → *Time-Dependent Solver* contain all the set-up fields to be changed if the default parameters differ. By default, the *Direct* robust solver node is offered. In this node one

can opt for three different solver types in *General* tab, depending on available computer resources. Here, the *PARDISO* was found to outperform the *MUMS* and *SPOOLS* solvers. Another important node to configure is the *Fully Coupled*. With this approach the results of one physics fully affect the other in multiphysics problem. In this node, the nonlinear method is the best to be set on *Automatic(Newton)* in *Method and Termination* tab with the rest parameters left unchanged. Moving one level up, several configurations must be also done in *Time-Dependent Solver* node. These are all the parameters in *Time Stepping* tab. First of all, for the BDF method selected, free steps taken by solver together with 1e-12 initial step are to be specified. Secondly, it is of good choice to fix the number 5 and 1 for Maximum and Minimum BDF order respectively. All of the mentioned solver settings and many others are listed in Table 3, Appendix B. On the whole, after configuring all of the aforementioned solver fields the optimization of the coupled PDEs solving must be achieved.

3.5 Computational domain and model settings

Most of the settings and parameters for simulation of corona currents under triangular voltages are given and explained in Section 3.4. Some necessary modifications of the model though will be presented in the current Section.

For large scale coaxial geometry used in experimental setup and described in Section 2.2, the computational domain is symmetric and 1D representation is enough for accurate result. Thus, in *Geometry* node under *Model* subgroup the interval geometry element should be selected with specified left and right endpoints of 0.00013 and 0.5 m respectively.

In *Global Definitions* node the *Waveform* function must be added for specifying the parameters of the triangular shape potential applied to the wire. In particular, the *Triangle* type with *Smoothing* set to 0.001 must be selected in *Parameters* tab. As for the angular frequency, $2*\pi*f$ must be indicated where f is waveform frequency that is subject to vary according to the experiment. The amplitude of the waveform can be either left at the default value 1 and controlled as a variable named, for example, *wave* with expression string $amp*potential(t)$, or directly specified in the *Amplitude* field. In the former option, one should create a constant named *amp* for indicating the amplitude of the waveform and name the *Waveform* function *potential* that, according to the aforementioned expression string, uses time t as an argument. The triangular waveform for 20 kV amplitude and 50 Hz frequency, implemented as waveform function, is plotted in Fig. 3.7. Fig. 3.8 shows the transition zone at the tip of the waveform, that in this case set to 0.001.

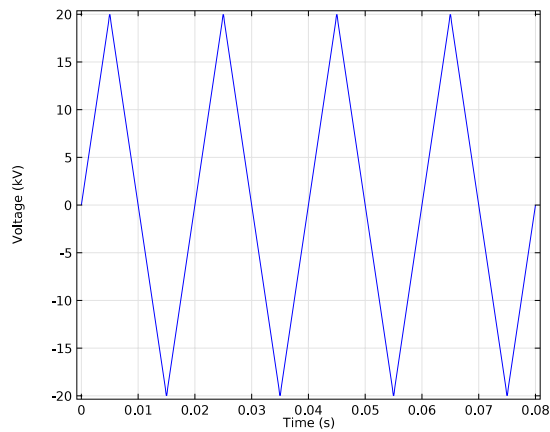


Fig. 3.7 Triangular voltage waveform: 20 kV, 50 Hz

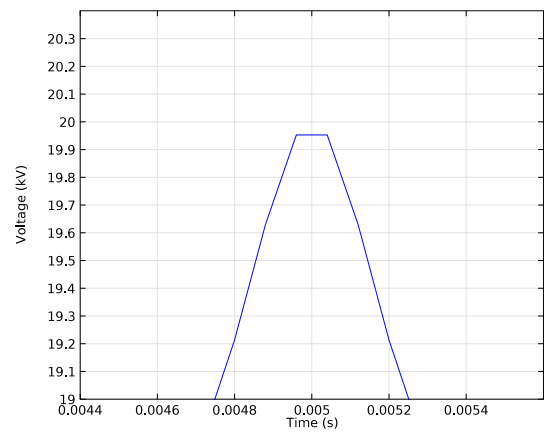


Fig. 3.8 Transition zone at the triangular waveform tip

The created waveform function is further used in *Electrostatics* interface to specify the Electric Potential applied to the wire.

Another modification specific to the alternating voltage corona discharge modelling is the current calculation approach. For this, in the *Definitions* subgroup one can create new *Variables* node for the entire model, where all the related expressions for current calculation are to be specified according to the theory presented in Section 3.2. Thus, the variable named *I_tot_cage_corr* in Fig. 3.9 is the implementation of the formula given in (3.23) for the total (compensated) current measured at the cage of the coaxial electrode arrangement.

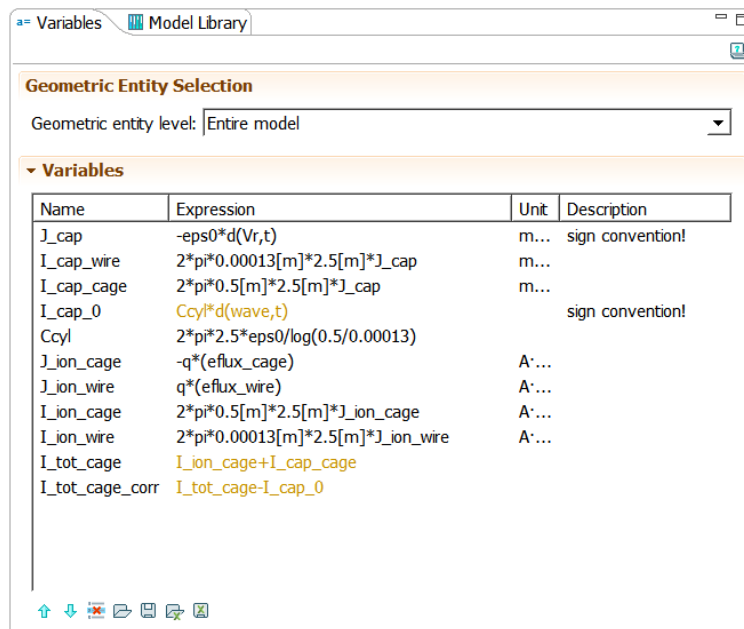


Fig. 3.9 Variables and expressions specified in Definitions node for current calculation

The total current indicated as the source for the y axes together with potential waveform function as the source for the x axes will generate the current-voltage characteristic of the corona discharge, being set up as the *Point Graph* in *ID Plot Group* of the *Results* subgroup.

Besides the *Variables* node for the entire model, two extra *Variables* nodes must be created at the *Definitions* subgroup, that will provide the information regarding electric field value at the boundary, one for the wire and the other one for the cage. For this, the *Geometric entity level* field must be selected as *Boundary* for each of the two nodes. For convenience purpose, the variable nodes can be renamed to *boundary_wire* and *boundary_cage* accordingly. At the *Name* field of the variables one can specify, for example, *Es_w* for the wire and *Es_c* for the cage. These boundary variables are to be used in logical expressions for the particles convective fluxes movement at the boundaries.

The boundary conditions in computational domain are to be specified by the logical expressions defined either globally or locally. There are six logical expressions, three for each boundary embracing three different species of particles. All the expressions defined globally are listed below

for negative ions at the cage boundary:

$$\text{nflux_in} + (-\text{nflux_in} + \text{nflux_out}) * (\text{mod1.Esc} > 0)$$

for positive ions at the cage boundary:

$$\text{pflux_in} + (-\text{pflux_in} + \text{pflux_out}) * (\text{mod1.Esc} < 0)$$

for electrons at the cage boundary:

$$\text{eflux_in} + (-\text{eflux_in} + \text{eflux_out}) * (\text{mod1.Esc} > 0)$$

for negative ions at the wire boundary:

$$\text{nflux_in} + (-\text{nflux_in} + \text{nflux_out}) * (\text{mod1.Esw} > 0)$$

for positive ions at the wire boundary:

$$\text{pflux_in} + (-\text{pflux_in} + \text{pflux_out}) * (\text{mod1.Esw} < 0)$$

for electrons at the wire boundary:

$$\text{eflux_in} + (-\text{eflux_in} + \text{eflux_out}) * (\text{mod1.Esw} > 0)$$

Here, *nflux_in* and *nflux_out* denote the conductive fluxes of negative ions with particular sign depending on whether ions inflow or outflow the boundary. The same applies to the fluxes of positive ions and electrons. Therefore, according to the expressions, the sign of an electric field at the boundary controls the direction of the particles movement. If the electric field is positive, the convective flux of the negative ions inflows the boundaries. No inward or outward flux exists for the negative ions at the boundaries once electric field becomes negative. The opposite works for positive ions. As for the electrons, these behave the same way as negative ions except that for negative electric fields the boundary expressions provide the mechanism of secondary ionization through incorporating γ coefficient. The necessary constants that will help to analyze the syntax in the logical expressions can be obtained from Fig. 3.6. Ultimately, the names given for the logical expressions are to be used for specification of inward fluxes in *Transport of Diluted Species* interfaces, one Flux node for each boundary in each particle type interface.

Chapter 4

Simulations of corona discharges in a large scale geometry

4.1 Model validation

Now, when the computer model based on theory described in Sections 3.1 through 3.3 has been implemented in COMSOL according to Sections 3.4 and 3.5, the first simulation results can be obtained and analysis made on several plots.

It is quite illustrative to use 50 Hz triangular voltage for the model validation and analysis. To begin with, the first four periods of the current-voltage characteristic shown in Fig. 4.1 can be studied. The discharge periods are intentionally separated by different line types. It is clear that the first period gives small magnitude of a discharge current due to space charge created by positive and negative ions in a discharge process.

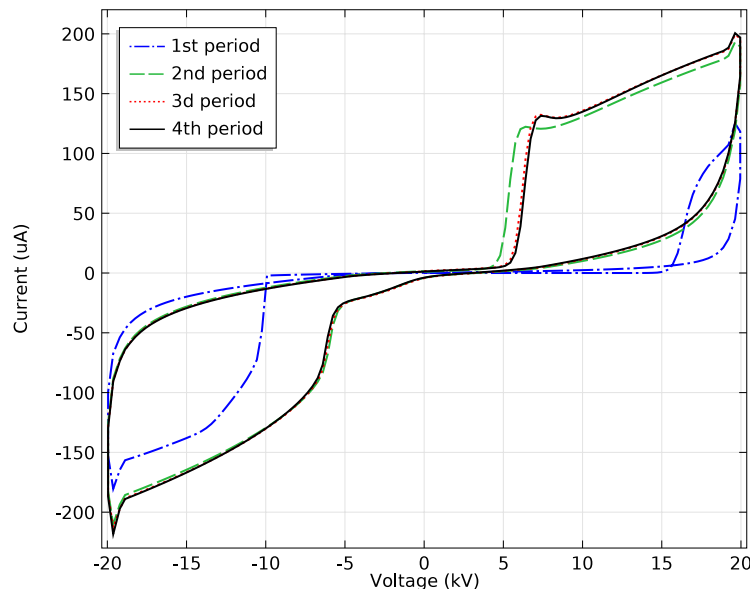


Fig. 4.1 Discharge current for 50 Hz triangular voltage (first 4 full periods)

However, the background ionization value and initial concentration of ions artificially introduced into the computation domain certainly affects the shape of the current in the first period. Positive and negative ions accumulate in an inter-electrode space forming

the space charge that oscillates under alternating potential. The space charge affects the corona onset voltage as well as the magnitude of a displacement current. It was noticed that first four cycles were enough to reach the so called steady state in a discharge process when all the subsequent discharge cycles were identical to the fourth one.

Another illustrative plot is given in Fig. 4.2. It is the discharge current decomposed into three components described in Section 3.2. One may notice that the capacitive current has bounds at the corners. According to (3.21) the derivative of the applied triangular voltage should result in a capacitive current being a horizontal line at maximum and minimum values resembling parallelepiped. The bounds, however, arise from the voltage transition function used to smooth the tip of the triangular wave. The application of the smoothing function has been described in Section 3.5. The shape of the voltage tip also affected the displacement current. It is logical to conclude that the same transition zone over the tip of a triangular wave potential has been present in the experiment. Thus resemblance of the experimental current-voltage characteristic and the one obtained by the simulation can be justified in the aforementioned zone.

As for the conductive current component, it was found to give zero contribution meaning that no charge carriers had been flowing into the cage electrode through the amperemeter circuit.

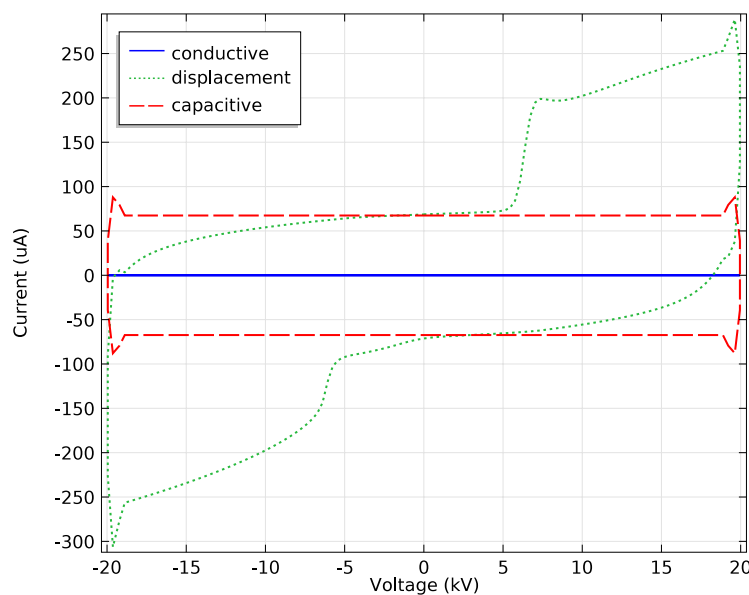


Fig. 4.2 Discharge current components

The plot of reduced electric field variation at the electrode surfaces, shown in Fig. 4.3, explains the behavior of a space charge yet reveals the problematic nature of a computation for such simulation problem. The space charge that accumulates during discharge cycles retards the electric field zero crossing at the cage electrode. The time difference in zero crossing between two electrodes is growing with the growing space charge until the size of latter reaches steady state, in this case the fourth period and later. During the positive half-cycle positive ions move towards the cage reaching the furthest point when the applied voltage changes sign. Therefore, while the negative applied voltage immediately changes the sign of the electric field at the wire, it takes some time for the positive ions to reverse their movement direction and let the electric field at the cage to be negated

by electrostatic conditions. The presence of a positive space charge in a proximity of the cage keeps the electric field positive in the weak field region irrespective of applied voltage sign. The same behavior is observed during negative half-period involving negative ions. The length of the weak field region and non-uniformity of the field distribution for the simulation electrode arrangement can be observed in Fig. 4.4.

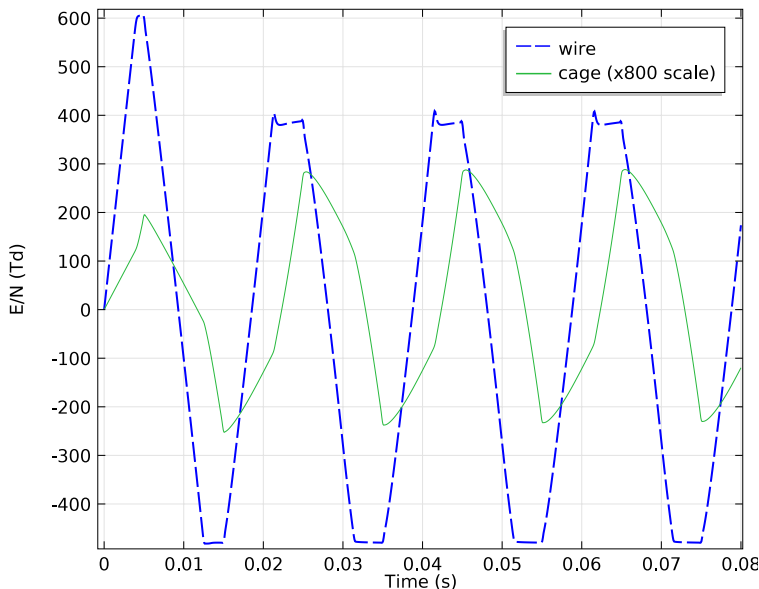


Fig. 4.3 Reduced electric field variation at the electrode surfaces

One may also notice the characteristic bound of electric field in the beginning of discharge process in each positive half-period. This bound is caused by local enhancement of electric field in ionization region when negative ions approach the wire. It is just a concurrence of time and spatial position of negative ions that leads to such bound in a positive half-period and not in a negative. Consequently, the bound in an electric field will be reflected on a corona discharge current.

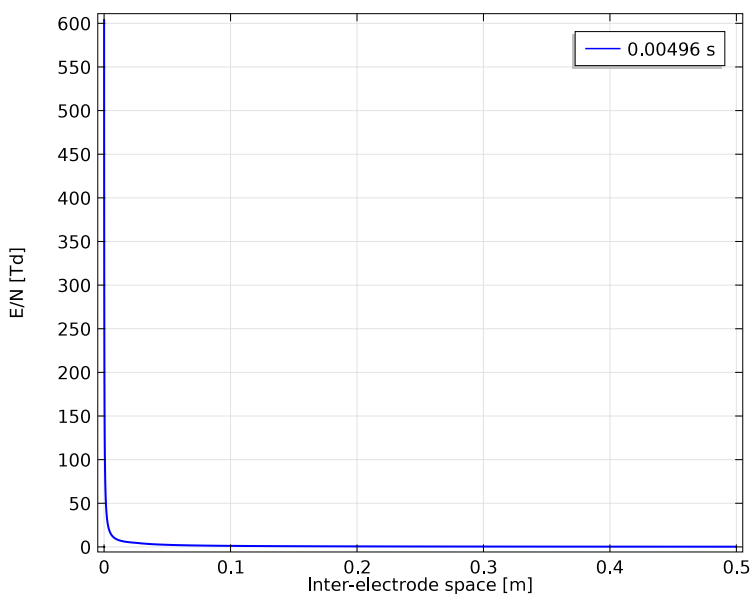


Fig. 4.4 Reduced electric field distribution (at first peak of 50 Hz waveform)

The zero crossing of the fields at the electrodes were noticed to be the cause for computation slow down. Zero field in the computation domain simply means zero velocity for the charge carriers. Approaching zero field makes solver to considerably decrease the time step taken to produce solution. Unfortunately, the zero crossing of the field is unavoidable and therefore such simulation of the corona discharge under alternating voltages takes great resource of time. In total, it was noticed that 80% of the computation time was spent on the solver finding solutions at zero field approaches.

Additionally, simulation for 1 Hz waveform showed inconsistency of the applied boundary conditions and resulted in computation errors. According to the boundary logical expressions given in Section 3.5, positive electric field at the cage makes the cage side boundary blocked for positive ions to cross it. The same has been applied to negative ions with negative electric field at the boundary. Such conditions worked perfectly well for all the frequencies except 1 Hz. At low frequencies when ions are able to cross the inter-electrode space in half-period, in a proximity of the cage they automatically block the boundary with positive field and their excessive piling up at the cage occurs. The piling up of the ions at the boundary results in sharp gradients of the concentrations and ultimately solver stalls with computation error. There is no piling up at the ground electrode in real physics and therefore more time should be spent on elaborating sophisticated boundary conditions allowing to avoid aforementioned problem.

To visualize the dynamics of ions, plots of their concentrations in the gap are shown in Fig. 4.5 through 4.8. The curves of ion concentrations correspond to the time instants at zero voltage, so that relative position of ions can be clearly seen for different wave periods. The growth of concentration is observed from first to fourth period. The growth of ions concentration justifies the growth of the displacement current magnitude from period to period, shown in Fig. 4.1. As was mentioned earlier, the size of the space charge formed by positive and negative ions reaches steady state at fourth wave period resulting in identical discharge current curves for later periods.

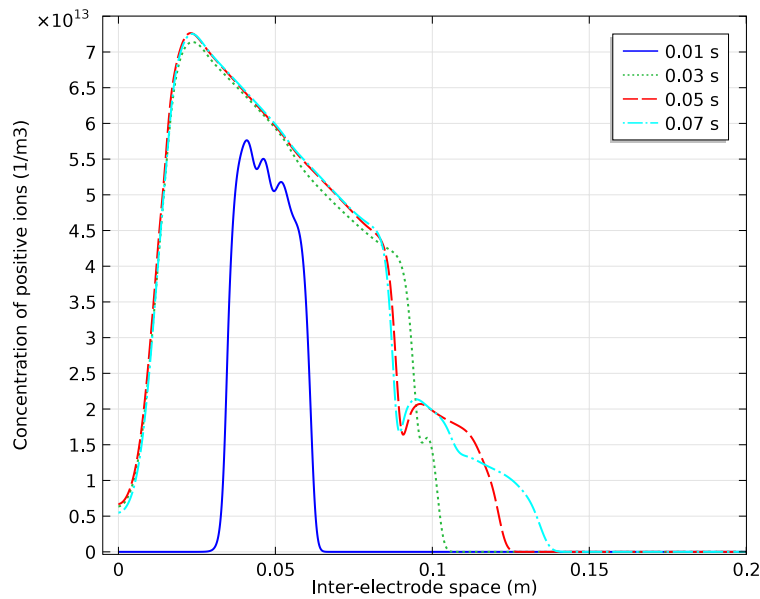


Fig. 4.5 Concentration of positive ions at zero voltage (50 Hz)

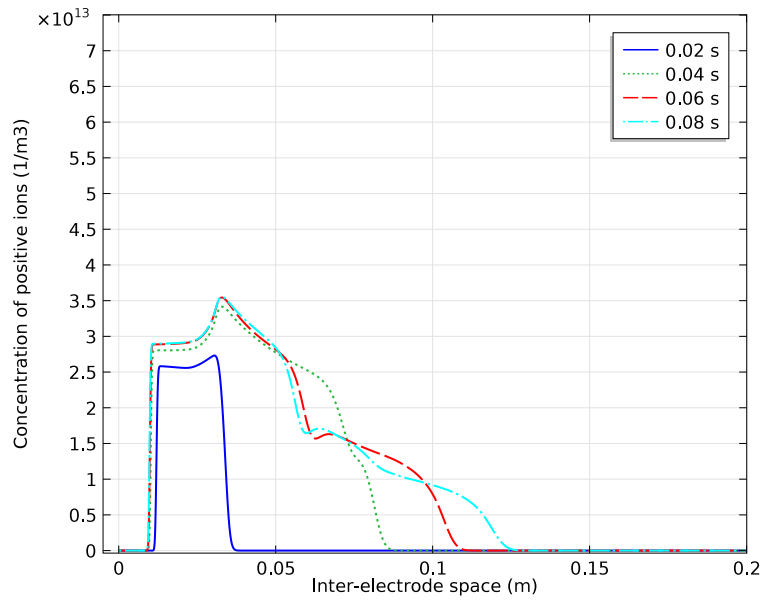


Fig. 4.6 Concentration of positive ions at zero voltage (50 Hz)

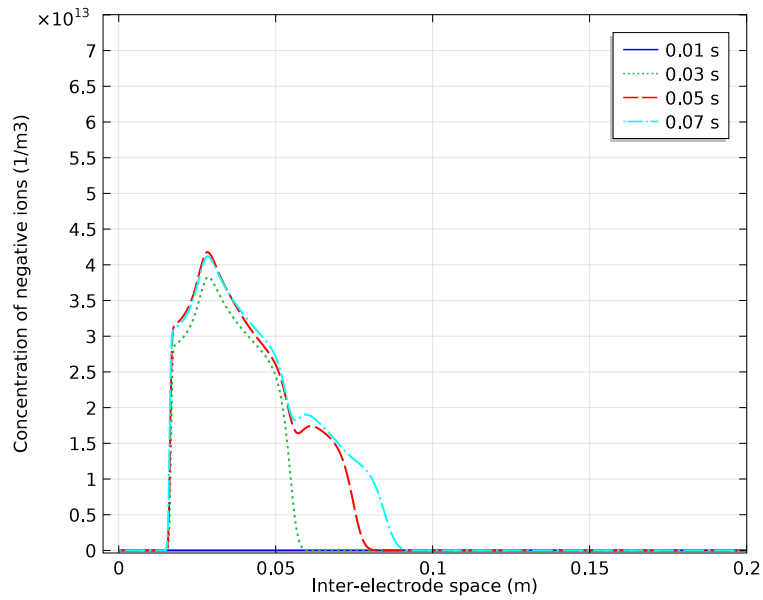


Fig. 4.7 Concentration of negative ions at zero voltage (50 Hz)

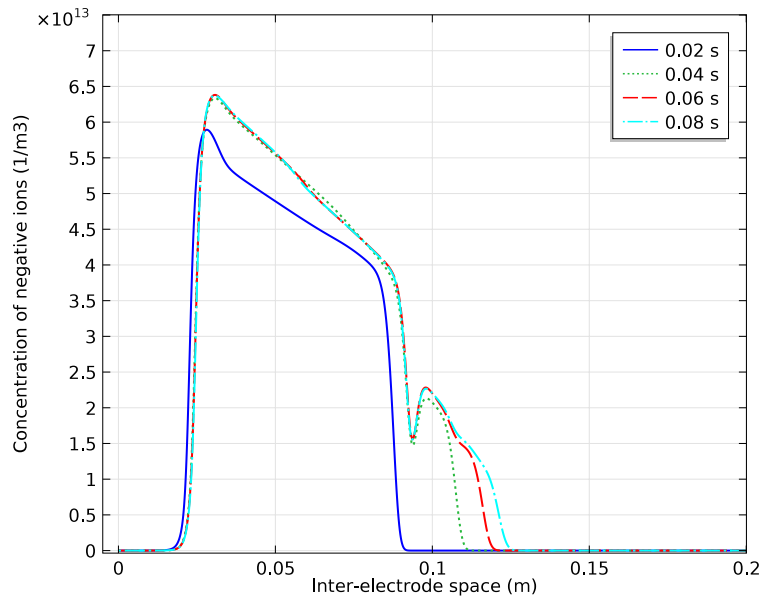


Fig. 4.8 Concentration of negative ions at zero voltage (50 Hz)

The presented characteristics in this Section proved the consistency of the developed simulation model. The boundary conditions were successfully verified for 50, 20, 10 and 5 Hz voltage waveforms. Simulations for 1 Hz and lower frequencies, however, should be performed with more sophisticated boundary conditions that will reflect the real physics of the ion interaction with electrode surfaces.

4.2 Sensitivity to variations of input parameters

Prior to comparison of the experimental results, presented in Section 2.2, with the simulation, the series of tests that reveal the sensitivity of the model to different input parameters need to be performed. These parameters, however, are limited by absolute value variation range. The range for parameter variation comply to the ranges stated in the literature by different scholars.

Among the parameters that affect the voltage current characteristic shape, the ion-ion recombination β_{ii} , detachment k_{det} , gamma γ coefficients together with positive μ_p and negative μ_n ion mobilities were selected. All the tests were performed for 50 Hz triangular voltage for the reason of the most characteristic shape of its CVC.

The formula for ion-ion recombination rate in atmospheric pressure air reported in [14] and reproduced in (3.24) for this particular test will appear in the following form

$$\beta_{ii} = k \cdot 10^{-12} \left(\frac{300}{T_i} \right)^{1.5} [m^{-3}s^{-1}] \quad (4.1)$$

where k substitutes the constant value in (3.24) and is subject to be varied in the following test.

The results of the variation of parameter k in (4.1) are plotted in Fig. 4.9

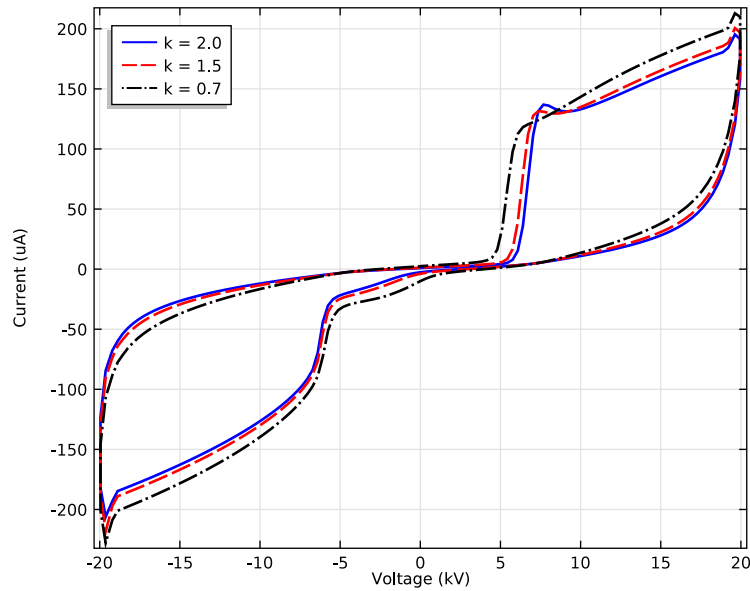


Fig. 4.9 Corona CVC. Sensitivity to ion-ion recombination coefficient

The formula for calculation of detachment coefficient, reported in [16] and given in (3.25) will take following form

$$k_{det} = k \cdot 10^{-16} \exp\left(-\frac{6030}{T_i}\right) [m^{-3}s^{-1}] \quad (4.2)$$

here, parameter k is subject to be varied.

Performing the test on detachment coefficient it has been revealed that the value of k in (4.2) that originally equaled 2 in (3.25) was too high to yield coherent result. The reason for lowering the parameter k in (4.2) is the previous assumption that detachment of electrons from the negative ions would occur due to collision of negative ions with the gas molecules. Obviously, this assumption had been giving too high values of detachment rate. Thus, the parameter k was greatly reduced meaning simply that not all the molecules dislodge the electrons from the negative ions.

Results illustrating the effect of parameter k in (4.2) are plotted in Fig. 4.10.

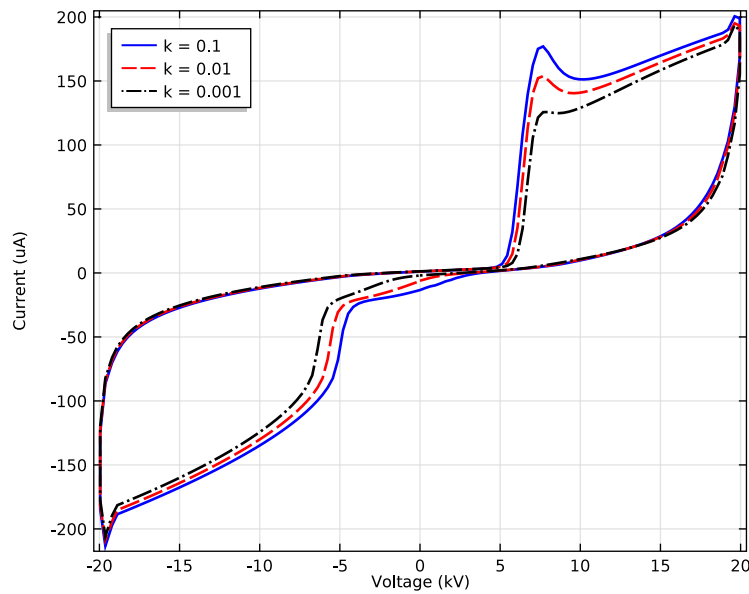


Fig. 4.10 Corona CVC. Sensitivity to detachment coefficient

The gamma coefficient γ that is used to describe the second ionization effect was another effective parameter that affected the shape of the corona discharge CVC. The values of γ were justified in Section 3.3. The resultant curves of CVC affected by variation of γ are plotted in Fig. 4.11.

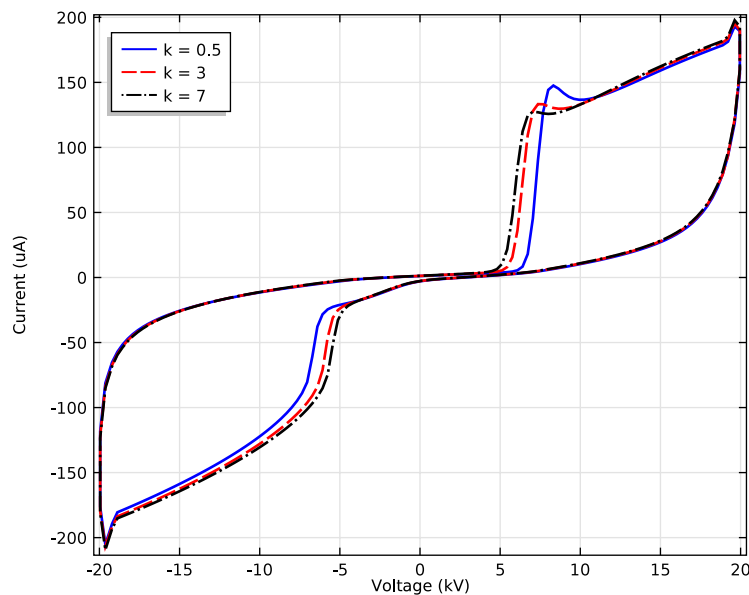


Fig. 4.11 Corona CVC. Sensitivity to gamma coefficient

Different authors reported rather scattered values for ion mobilities in atmospheric pressure air. This may be attributed to different equipment used and experiments conditions. The studies reveal that the mobility of negative ions is greater than that of the positive, therefore, this condition is to be preserved in the current simulations. Equally important was to consider the lower and the upper reported values of ion mobilities. These limits are also taken into account in the tests. Fig. 4.12-4.13 illustrate the affect of ion mobilities on corona CVC. The mobility values tested are given in the legend and denoted as

parameter k .

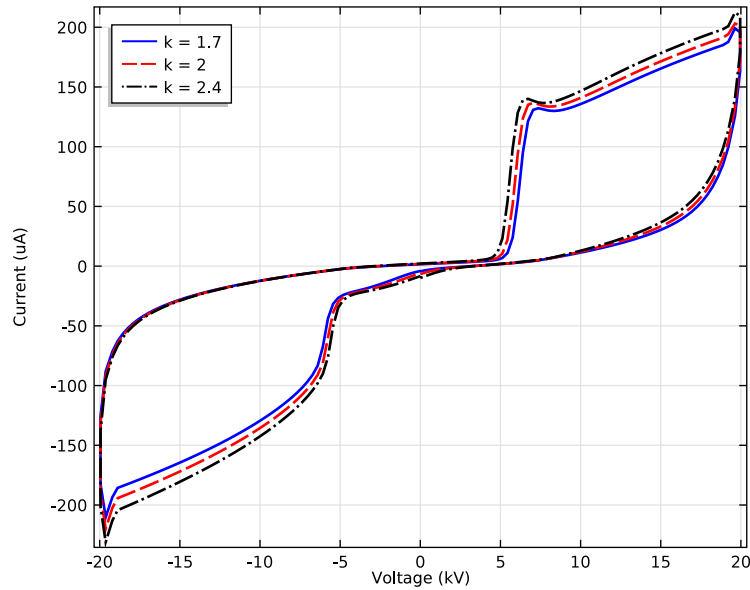


Fig. 4.12 Corona CVC. Sensitivity to negative ion mobility

From Fig. 4.12 two distinctive effects may be concluded. First, increased negative ion mobility gives higher amplitude of the current at positive half-periods. This is due to lower amount of negative ions involved in recombination processes thus leaving higher concentration of positive ions affecting electric field that eventually increases the displacement current. At the negative half-period the magnitude of the current may be affected by longer distances ion travel at higher mobilities thus creating larger area of dynamically changing electric field. Second, greater mobility of negative ions lowers the corona onset voltage in positive half-period. This is due to faster return of the residual negative ions to the wire after negative half-period. This faster return causes the enhancement of electric field near the wire and thus ionization kicks off at lower potential.

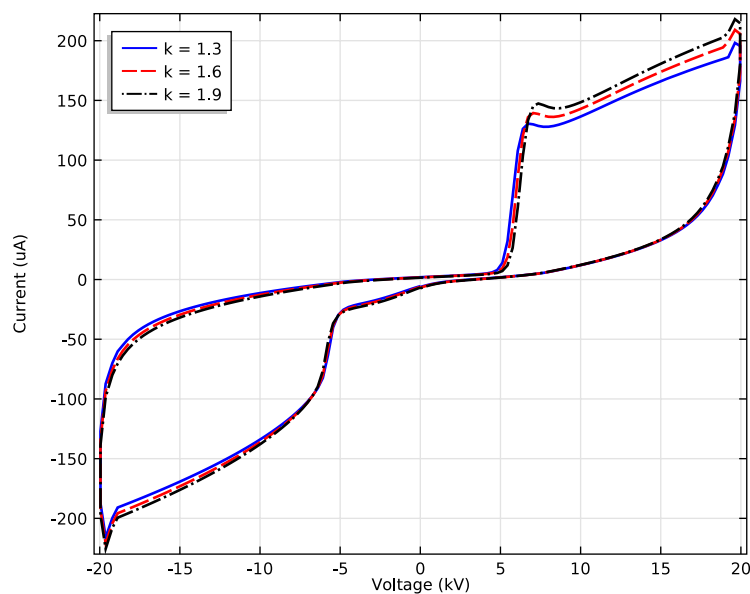


Fig. 4.13 Corona CVC. Sensitivity to positive ion mobility

In case of positive ion mobility variation plotted in Fig. 4.13 there is only one prominent effect visible at the positive half-period. The increased positive ion mobility allows for larger area of the space charge spreading that in turn increases the displacement current.

4.3 Corona current-voltage characteristics: experiment vs. simulation

After the sensitivity analysis of the model has been performed, the parameters that the model was the most sensitive to, were adjusted to achieve the match between the experimental and simulation results. It was assumed that there could be no difference in parameters simulating for different frequencies. Therefore, once fixed at the desired value testing for 50 Hz wave, the same parameters of the model were used to produce the corona discharge curves for other frequencies.

The best fit of the simulation curves to the experimental ones has been achieved by altering the parameters summarized in Table 4.1.

Table 4.1: Modified parameters of the model

Parameter	Units	Value in literature	Modified value
Positive ions mobility, μ_p	$\frac{m^2}{V \cdot s}$	$2.0e^{-4}$	$1.5e^{-4}$
Negative ions mobility, μ_n	$\frac{m^2}{V \cdot s}$	$2.7e^{-4}$	$1.7e^{-4}$
Secondary ionization coeff., γ		$1e^{-3}$	$2e^{-5}$
Detachment rate coeff., k_{det}	$\frac{m^3}{s}$	$2e^{-16} \cdot \exp\left(-\frac{6030}{T_n}\right)$	$2.5e^{-19} \cdot \exp\left(-\frac{6030}{T_n}\right)$
Ion-ion recombination rate, β_{ii}	$\frac{m^3}{s}$	$2e^{-12} \left(\frac{300}{T_i}\right)^{1.5}$	$1.5e^{-12} \left(\frac{300}{T_i}\right)^{1.5}$

Among the parameters listed only ion-ion recombination rate has been modified to exceed the value stated in literature. In general, there was no reference found suggesting possible variation of reaction rates.

The modified values of ions mobilities and secondary ionization coefficient yielded satisfactory result being selected within the range reported by already referenced scholars [12] [11]. The detachment rate was greatly reduced in reference to the literature value due to the detachment mechanism assumed in the simulation model. The simulation has shown that association of all gas molecules N in the detachment process yielded excessive number of electrons in the gap, that distorted the discharge current shape too much to be fitted to the experimental case.

The match between obtained current-voltage characteristics using modified parameters from Table 4.1 and experimental curves are shown in Fig. 4.14 through 4.17. One

4.3. Corona current-voltage characteristics: experiment vs. simulation

may refer to Table 3 in Appendix B as well in order to realize how much time it took to produce the simulation results for each of the frequencies.

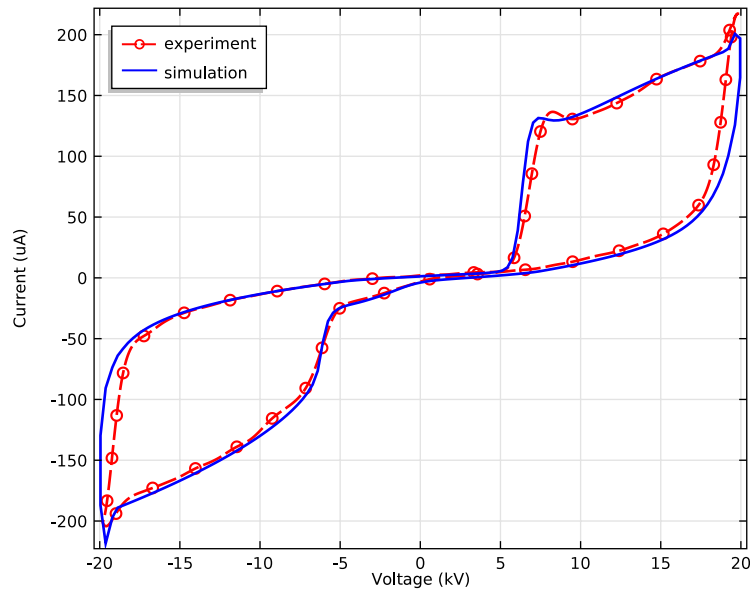


Fig. 4.14 Corona current-voltage characteristic for 50 Hz triangular voltage

Looking at the experimental and simulation curves in Fig. 4.14 few clarifications can be made. First, none of the parameters were found affecting the slope of the current rise in the region after the corona onset. Second, none of them were changing the shape of the curve in the current decrementing region after the corona peak. Therefore, much of the deviation is observed in these particular regions for 50 Hz CVC. This deviation becomes less profound for other frequencies.

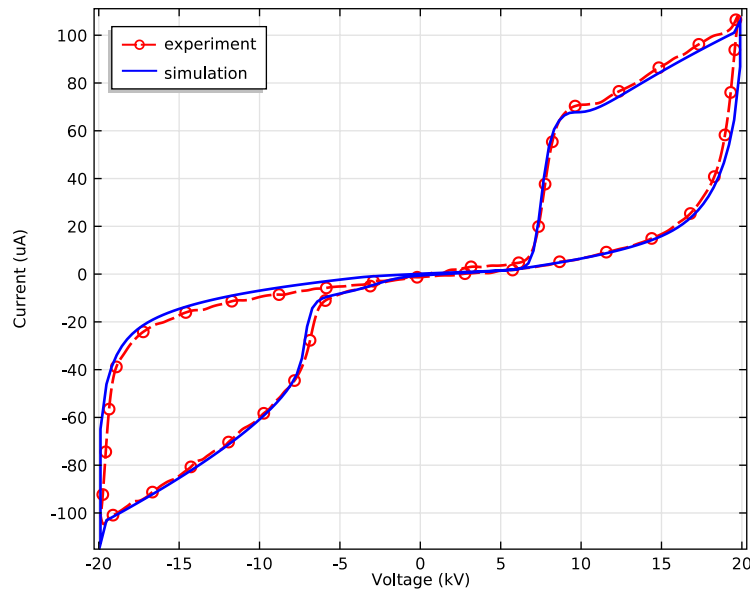


Fig. 4.15 Corona current-voltage characteristic for 20 Hz triangular voltage

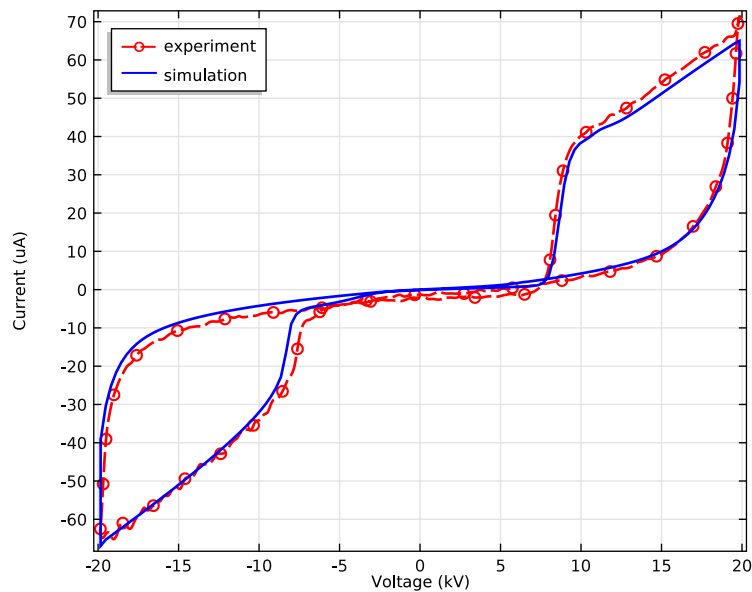


Fig. 4.16 Corona current-voltage characteristic for 10 Hz triangular voltage

The match plotted in Fig. 4.17 reveals inaccuracy in the experimental data as well. Unfortunately, no rigid statements concerning the quality of the experimental results can be made due to the unique set of experimental data available for each of the frequencies. Up to a point, there was simply no possibility to select the most accurate data set for the comparison purpose. Records of the potential wave applied to the electrode in the experiment could shed some light on the matter as well.

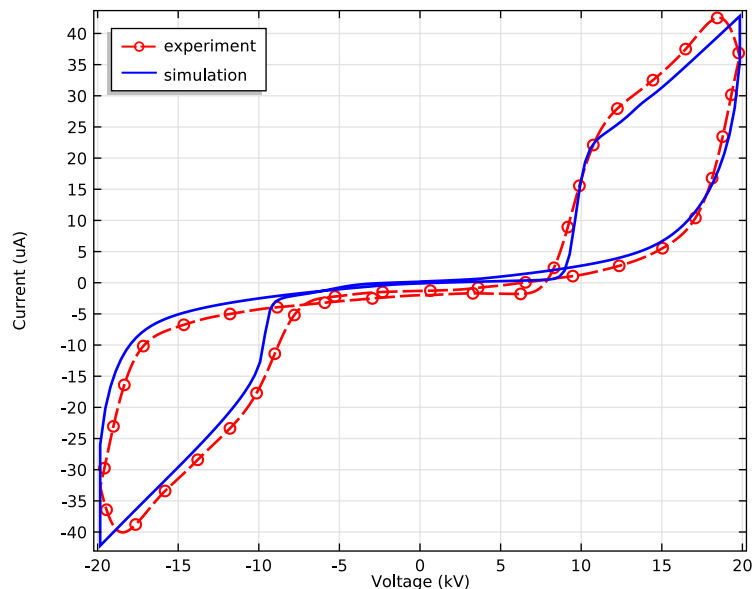


Fig. 4.17 Corona current-voltage characteristic for 5 Hz triangular voltage

It is believed that the voltage waveform used in the experiment being compared with the one used in the simulation could give the answers to why some of the curves match perfectly well and others do not. Without sufficient data from the experiment, it is impossible to conclude whether the model restriction in terms of incomplete set of reactions accounted for between electrons and ions, is responsible for discrepancies.

4.3. Corona current-voltage characteristics: experiment vs. simulation

On the whole, there was no attempt to justify exact values of listed modified parameters for the conditions used in the experiment. Hence, the presented fit of the simulation curves to the experimental ones is considered satisfactory 'as is' with all the resources available.

Chapter 5

Conclusions

After completion of the corona simulations and analysis for the large scale coaxial geometry several findings can be summarized.

The unavailability of electron swarm parameters measured in a broad range of electric field for different levels of air humidity and usage of those for dry air instead brings certain inaccuracy into simulation results. Though the swarm parameters of ions had been adjusted to the predefined air relative humidity and pressure value.

The computer implementation and simulation of the AC corona in COMSOL Multiphysics made it possible to scrutinize the physics of discharge plasma for the experimental coaxial set-up. By plotting studying parameters in time, spatial and electric field domains the formation, transport and recombination processes for three generic types of charge carriers, electrons, positive and negative ions have been fully examined. Some of the plots have clearly illustrated the cause for the experimental current-voltage characteristics particulars such as the shape of the capacitive current, characteristic bound of discharge current at the positive half period, etc. In addition, the detailed sensitivity analysis of the corona parameters made it possible to achieve the best fit of the simulation current-voltage characteristics to the experimental ones. Besides that, the created and validated corona model for COMSOL may be fully utilized for simulation and analysis of AC corona discharges in different electrode arrangements and potential waveforms. Though, the applicability of the model is restricted.

Among numerous approximations and assumptions for the simplification of the corona simulation model, the boundary conditions as they were defined, proved inconsistency for 1 Hz and lower frequencies AC waveform simulation. The simple cage boundary conditional expression does not reflect the real physics of the ions association with the metallic surface of the grounded electrode. Therefore, at those frequencies where ions have time to traverse the inter-electrode space before being reversed by the applied voltage of the opposite sign, they get accumulated at the cage to extremely sharp concentrations resulting in computation errors.

The match of the experimental current-voltage characteristics with the ones obtained experimentally has revealed minor discrepancies in some of the regions of the discharge current. None of the parameters, unfortunately, were found to affect those particular regions. These discrepancies may be the consequence of the simulation model incompleteness in the sense of the particle reaction number accounted for. The availability of the triangular voltage waveform recorded data from the experiment plotted in time domain

for all the tests conducted could bring some clarity in finding the real cause for mentioned discrepancies.

After all, one should carefully consider the studying frequencies of the AC corona discharges utilizing the finite element method. In order to resolve corona currents with high accuracy the dense meshing of the geometry is needed. If it were not for coaxial electrode arrangement and 1D domain set-up, this type of the problem and research objectives set for the thesis would be treated unsolvable by means of COMSOL Multiphysics.

5.1 Future work

In order to utilize the developed model for low frequency discharges, it is suggested to modify the boundary conditions that will allow to avoid computation errors due to unnatural high concentrations at the cage electrode. Additionally, one can elaborate the current model to study the effect of air pressure and humidity on corona discharges under alternating voltages. Having this realized, will allow to get more accurate results simulating for different air conditions and also make the model applicable to solve relative equipment design problems.

References

- [1] J M Meek and J D Craggs, editors. *Electrical Breakdown of Gases*. John Wiley & Sons, 1978.
- [2] L B Loeb. *Electrical coronas, their basic physical mechanisms*. University of California Press, 1965.
- [3] J J Lowke. Theory of electrical breakdown in air - the role of metastable oxygen molecules. *Journal of Physics D: Applied Physics*, 25, September 1991.
- [4] G G Raju. *Gaseous Electronics. Theory and Practice*. CRC Press, 2006.
- [5] H Ryzko. Ionization, attachment and drift velocity of electrons in water vapour and dry air. *Arkiv f. Fysik*, 32:1–18, 1966.
- [6] E Kuffel. Electron attachment coefficients in oxygen, dry air, humid air and water vapour. *Proc. Phys. Soc.*, 74:297–308, 1959.
- [7] H Ryzko. Drift velocity of electrons and ions in dry and humid air and in water vapour. *Proc. Phys. Soc.*, 85:1283–1295, 1965.
- [8] Mazen Abdel-Salam. Positive Wire-to-Plane Coronas as Influenced by Atmospheric Humidity. *IEEE Transactions on Industry Applications*, IA-21(1), January 1985.
- [9] Xingming Bian, Liming Wang, J M K MacAlpine, Zhicheng Guan, et al. Positive Corona Inception Voltages and Corona Currents for Air at Various Pressures and Humidities. *IEEE Transactions on Dielectrics and Electrical Insulation*, 17(1), February 2010.
- [10] Xingming Bian, Xiaobo Meng, Liming Wang, et al. Negative Corona Inception Voltages in Rod-plane Gaps at Various Air Pressures and Humidities. *IEEE Transactions on Dielectrics and Electrical Insulation*, 18(20), April 2011.
- [11] J J Lowke and F D'Alessandro. Onset corona fields and electrical breakdown criteria. *Journal of Physics D: Applied Physics*, October 2003.
- [12] L G Huxley and R W Crompton. *The diffusion and drift of electrons in gases*. Wiley, 1974.
- [13] U Horrak, H Iher, A Luts, et al. Mobility spectrum of air ions at Tahkuse Observatory. *J. Geophys. Res. Atmospheres*, 99, 1994.

References

- [14] B M Smirnov. *Negative Ions*. McGraw-Hill, 1982.
- [15] G V Naidis. *Journal of Physics D: Applied Physics*, 32(20), 1999.
- [16] A Kh Mnatsakanyan and G V Naidis. *Reviews of Plasma Chemistry*. 1.

Appendices

Appendix A

Table 1: Reduced ionization α/N and attachment η/N coefficients, electron velocity W and characteristic energy D_e/μ as a function of reduced electric field E/N for dry air (published by J.J. Lowke [3] and G.G. Raju [4])

E/N (Td)	η/N (m ²)	E/N (Td)	η/N (m ²)	E/N (Td)	D_e/μ (eV)	E/N (Td)	W (m/s)
95	1.00E-24	0.00	6.00E-22	2	0.29	0.3	3600
100	2.00E-24	0.99	4.95E-22	3	0.4	0.4	4000
110	2.00E-23	1.94	2.46E-22	5	0.62	0.6	4910
120	6.20E-23	2.77	1.62E-22	8	0.85	0.8	5780
125	7.30E-23	3.63	1.15E-22	10	0.95	1	6580
150	1.85E-22	4.73	8.10E-23	16.5	1.15	2	9520
175	3.06E-22	6.37	5.93E-23	20	1.25	3	11360
200	5.21E-22	9.67	3.83E-23	30	1.26	4	12760
250	1.09E-21	13.34	2.67E-23	40	1.3	6	15500
300	1.99E-21	18.64	1.91E-23	50	1.35	8	18260
350	2.65E-21	26.19	1.39E-23	70	1.6	10	21000
400	3.68E-21	37.46	1.13E-23	100	2.15	20	38000
450	4.58E-21	44.41	1.07E-23	200	4	30	50000
500	5.49E-21	51.42	1.12E-23	300	5.25	100	122000
600	7.60E-21	61.70	1.48E-23	400	6.5	200	200000
700	9.08E-21	75.35	2.08E-23	500	7.5	300	267000
800	1.09E-20	90.94	2.78E-23	600	8.6	400	323000
900	1.33E-20	104.71	3.45E-23	700	9.5	500	380000
1000	1.43E-20	117.77	3.88E-23			600	439000
1100	1.51E-20	138.81	4.18E-23			700	494000
1200	1.71E-20	166.51	4.22E-23				
1300	1.87E-20	213.04	3.99E-23				
1400	1.98E-20	249.60	3.53E-23				
1500	2.06E-20	319.32	2.97E-23				
1600	2.17E-20	401.39	2.48E-23				
1700	2.29E-20	504.55	2.09E-23				
1800	2.40E-20	608.73	1.84E-23				

Table 2: Characteristics of hardware used for simulations

Processor: Intel(R) Core i7-2600K 3.4 GHz
RAM: 32 GB

Appendix B

Table 3: PARDISO solver settings and approximate time spent on calculations of corona for 4 full periods of triangular voltage

Solver settings	
Time stepping configuration	
Method	BDF
Steps taken by solver	Free
Initial step	1E-12 (check)
Maximum BDF order	5
Minimum BDF order	1
Event tolerance	0.00001
Direct entry configuration	
Type	PARDISO (Time-Dependent)
Preordering algorithm	Nested dissection multithreaded
Scheduling method	Auto
Row preordering	Check
Check error estimate	Automatic
Fully Coupled entry configuration	
Linear solver	Direct
Nonlinear method	Automatic (Newton)
Initial damping factor	1
Minimum damping factor	1.0E-4
Restriction for step size update	10
Use recovery damping factor	Automatic
Recovery damping factor	0.75
Termination technique	Tolerance
Maximum number of iterations	10
Tolerance factor	1
Time for simulation frequencies	
50 Hz	approx. 5 hours
20 Hz	approx. 8 hours
10 Hz	approx. 12 hours
5 Hz	approx. 16 hours